Journal of Materials Chemistry A

Colloidal Ni2-xCoxP nanocrystals for the hydrogen evolution reaction

Journal:	*Journal of Materials Chemistry A*
Manuscript ID	TA-ART-04-2018-003485
Article Type:	Paper
Date Submitted by the Author:	16-Apr-2018
Complete List of Authors:	Liu, Junfeng; Catalonia Institute for Energy Research, Advanced Materials Wang, Zhenxing; Xi'an Jiaotong University David, Jeremy; Catalan Institute of Nanoscience and Nanotechnology (ICN2) Llorca, Jordi; Technical University of Catalonia, Institute of Energy Technologies Li, Junshan; Catalonia Institute for Energy Research (IREC) Yu, Xiaoting; Catalonia Institute for Energy Research (IREC) Shavel, Alexey; Universitat de Barcelona, Arbiol, Jordi; Institut Català de Nanociència i Nanotecnologia (ICN2), CSIC and The Barcelona Institute of Science and Technology (BIST), Advanced Electron Nanoscopy (GAeN); ICREA, Meyns, Michaela; Catalonia Institute for Energy Research, Advanced Materials; Alfred-Wegener-Institute, Helmholtz Centre for Polar and Marine Research, Biologische Anstalt Helgoland Cabot, Andreu; Catalonia Institute for Energy Research, Advanced Materials

Institut de Recerca en Energia de Catalunya
Catalonia Institute for Energy Research

Advanced Materials Research Area
Functional Nanomaterials Group
Jardi de les Dones de Negre 1
08930, SantAdria del Besos, Barcelona (Spain)
Tel. +34 93 403 9154
Fax +34 93 402 11 48

Journal of Materials Chemistry A

April 16th, 2018

Dear Editor,

We are electronically submitting for your consideration as a potential article in the *Journal of Materials Chemistry A* the manuscript entitled "Colloidal $Ni_{2-x}Co_xP$ nanocrystals for the hydrogen evolution reaction" by Junfeng Liu, ZhenxingWang, Jeremy David, Jordi Llorca, Junshan Li, Xiaoting Yu, Alexey Shavel, Jordi Arbiol, Michaela Meyns and Andreu Cabot. This work has not been published previously, nor is it under consideration elsewhere.

In this article, we detail a cost-effective and scalable approach to produce monodisperse $Ni_{2-x}Co_xP$ nanocrystals (NCs) with composition tuned over the entire range ($0 \leqslant x \leqslant 2$). $Ni_{2-x}Co_xP$ NCs were synthesized using low-cost, stable and low-toxicity triphenylphosphite (TPP) as phosphorous precursor, metal chlorides as metal precursors and hexadecylamine (HDA) as ligand. The synthesis involved the nucleation of amorphous Ni-P and its posterior crystallization and simultaneous incorporation of Co. The composition, size and morphology of the NCs could be controlled simply by varying the ratio of Ni and Co precursors and the amount of TPP and HDA. Ternary $Ni_{2-x}Co_xP$ based electrocatalysts exhibited enhanced electrocatalytic activity toward hydrogen evolution reaction (HER) compared to binary phosphides. In particular, NiCoP electrocatalysts displayed the lowest overpotential of 97 mV at J=10 mA cm^{-2} and an excellent long-term stability. DFT calculations of the Gibbs free energy for hydrogen adsorption at the surface of $Ni_{2-x}Co_xP$ NCs showed NiCoP to have the most appropriate composition to optimize this parameter within the whole $Ni_{2-x}Co_xP$ series. However, the hydrogen adsorption energy was demonstrated not to be the only parameter controlling HER activity in $Ni_{2-x}Co_xP$.

We believe this contribution will be of high interest for the Journal of Materials Chemistry A community, especially for those researchers involved in the synthesis of nanocrystals and nanomaterials and particularly metal phosphides, and for those employing nanomaterials for energy conversion applications and particularly fuel cells.

Thank you for your consideration of this manuscript.

Sincerely,

Prof. Andreu Cabot
Advanced Material Research Department
Catalonia Institute for Energy Research - IREC
Phone: +34 625615115
acabot@irec.cat

Journal Name

ARTICLE

Colloidal $Ni_{2-x}Co_xP$ nanocrystals for the hydrogen evolution reaction

Received 00th January 20xx,
Accepted 00th January 20xx

DOI: 10.1039/x0xx00000x

www.rsc.org/

Junfeng Liu,[a] Zhenxing Wang,[b] Jeremy David,[c] Jordi Llorca,[d] Junshan Li,[a] Xiaoting Yu,[a] Alexey Shavel,[a] Jordi Arbiol,[ce] Michaela Meyns,*[a] Andreu Cabot*[ae]

A cost-effective and scalable approach was developed to produce monodisperse $Ni_{2-x}Co_xP$ nanocrystals (NCs) with composition tuned over the entire range ($0 \leqslant x \leqslant 2$). $Ni_{2-x}Co_xP$ NCs were synthesized using low-cost, stable and low-toxicity triphenyl phosphite (TPP) as phosphorous precursor, metal chlorides as metal precursors and hexadecylamine (HDA) as ligand. The synthesis involved the nucleation of amorphous Ni-P and its posterior crystallization and simultaneous incorporation of Co. The composition, size and morphology of the NCs could be controlled simply by varying the ratio of Ni and Co precursors and the amount of TPP and HDA. Ternary $Ni_{2-x}Co_xP$ based electrocatalysts exhibited enhanced electrocatalytic activity toward hydrogen evolution reaction (HER) compared to binary phosphides. In particular, NiCoP electrocatalysts displayed the lowest overpotential of 97 mV at J = 10 mA cm^{-2} and an excellent long-term stability. DFT calculations of the Gibbs free energy for hydrogen adsorption at the surface of $Ni_{2-x}Co_xP$ NCs showed NiCoP to have the most appropriate composition to optimize this parameter within the whole $Ni_{2-x}Co_xP$ series. However, the hydrogen adsorption energy was demonstrated not to be the only parameter controlling HER activity in $Ni_{2-x}Co_xP$.

Introduction

The development of highly active electrocatalysts not based on Pt or Pt-group metals (PGMs) for the HER in acidic conditions has become a priority to reduce cost and allow extensive commercialization of PEM fuel cells. In this direction, particular transition-metal phosphides are being evaluated as potentially viable alternative electrocatalysts.[1-14] Some transition metal phosphides are characterized not only by low cost and toxicity, but also excellent electrical conductivities and proper densities of states to allow an effective HER. While binary phosphides have reached performances relatively close to those of PGMs, ternary and multinary phosphides, with additional degrees of freedom to tune electronic band structure and surface chemistry, are expected to further close the gap with actual best HER catalysts.[15-21]

A crucial challenge that currently limits the use of metal phosphides in their wider range of applications is the lack of cost-effective approaches to produce nanostructures of these materials with properly adjusted properties. This limitation is particularly critical for multinary phosphides. Currently, multinary metal phosphide NCs are generally produced from the phosphorization of metal or metal oxide nanoparticles using toxic and expensive phosphorus sources such as phosphane, trioctylphosphine (TOP), (trimethylsilyl)phosphine (TMSP), as well as red/white phosphorus. As it involves two steps, this common strategy presents additional limitations in terms of cost and control of composition and structural parameters of multinary phosphides.

Among ternary phosphides, $Ni_{2-x}Co_xP$ has been demonstrated an excellent catalyst for HER and OER as well as an excellent electrode material for supercapacitor and lithium ion batteries.[22-29] Microstructured $Ni_{2-x}Co_xP$ has been synthesized through hydrothermal method by reacting metal chlorides with white phosphorus or NaH_2PO_2.[30,31] $Ni_{2-x}Co_xP$ has been also synthesized through annealing of Ni_xCo_y alloys within a phosphane gas atmosphere[22,23] or through the reaction of pre-formed colloidal Ni_xCo_y NCs with trioctylphosphine (TOP).[32,33]

We recently demonstrated triphenyl phosphite (TPP) as a cheap, stable and less-toxic phosphorous precursor that can be used to produce a range of binary metal phosphides.[34] Motivated by the expectation of expanding the use of TPP to the synthesis of ternary metal phosphides, we show here the possibility of producing $Ni_{2-x}Co_xP$ ($0 \leqslant x \leqslant 2$) NCs using metal chlorides and this phosphorus source. We further scaled up the synthesis procedure to the gram scale and tested these $Ni_{2-x}Co_xP$ NCs for HER in acidic solution. The performance of

[a] Catalonia Institute for Energy Research (IREC), Sant Adrià de Besòs, 08930 Barcelona, Spain
[b] IState Key Laboratory of Electrical Insulation and Power Equipment, Xi'an Jiaotong University, 710049, Xi'an, China
[c] Catalan Institute of Nanoscience and Nanotechnology (ICN2), CSIC and BIST, Campus UAB, Bellaterra, 08193 Barcelona, Catalonia, Spain
[d] Institute of Energy Technologies, Department of Chemical Engineering and Barcelona Research Center in Multiscale Science and Engineering, Universitat Politecnica de Catalunya, Eduard Maristany 10-14, 08019 Barcelona, Spain
[e] ICREA, Pg. Lluis Companys 23, 08010 Barcelona, Catalonia, Spain

† Electronic Supplementary Information (ESI) available: additional DFT calculation data, size distribution, HRTEM, EELS analysis and other characterizations, stability measurement. See DOI: 10.1039/x0xx00000x

these materials toward HER is analyzed as a function of the composition and explained using DFT calculations of the Gibbs free energy for hydrogen adsorption on the surface of these materials.

Experimental

Chemicals

Triphenyl phosphite (TPP, 99%) was purchased from Alfa Aesar. 1-Octadecene (ODE, 90%), hexadecylamine (HDA, technical grade 90%), nickel (II) chloride ($NiCl_2$, 98%), cobalt (II) chloride ($CoCl_2$, 98%) and hexafluorophosphoric acid (HPF_6, 65 wt%), carbon-supported Pt NCs (Pt/C, 10 wt% Pt) and Nafion (5 wt% in a mixture of low aliphatic alcohols and water) were purchased from Sigma Aldrich. Chloroform, isopropanol and acetone were of analytical grade and obtained from various sources. Milli-Q water was supplied by a PURELAB flex from ELGA. All precursors and solvents were used without further purification.

Synthesis of $Ni_{2-x}Co_xP$ NCs

All reactions were carried out under argon atmosphere using standard Schlenk line techniques. In a typical synthesis, the proper amount of $NiCl_2$ and $CoCl_2$ (overall 1.0 mmol) and 2.4 g (10 mmol) of HDA were combined with 10.0 mL of ODE and 2.6 mL (10 mmol) of TPP in a 50 mL flask equipped with a condenser. The system was heated to 150 °C under argon flow (30 mL min^{-1}) and maintained at this temperature for 1 h to remove low boiling point impurities, moisture and oxygen. The temperature was then increased to the solvent boiling point (about 290 °C) in 20 min and kept there for 1 h. Afterward, the mixture was allowed to cool down to 200 °C by removing the heating mantle and then cooled rapidly down to room temperature with a water bath. The black product was isolated by precipitation with acetone. To remove as much organics as possible, two redispersion and precipitation cycles using chloroform and acetone were additionally carried out.

The synthesis of $Ni_{2-x}Co_xP$ NCs was scaled up in a 500 mL flask containing 1.3 g (10 mmol) of $NiCl_2$ and 1.3 g (10 mmol) of $CoCl_2$, 52 mL (200 mmol) of TPP, 48 g (200 mmol) of HDA and 100 mL of ODE. The temperature was maintained at 150 °C for 2 h under argon flow and afterward increased to the solvent boiling point. After 2h reaction, the reaction mixture was cooled down and purified as detailed above.

Different sizes of spherical NiCoP NCs were prepared following the same procedure, using 65 mg (0.5 mmol) of $NiCl_2$ and 65 mg (0.5 mmol) of $CoCl_2$ but different amounts of TPP. Different morphologies were produced by tuning the amount of HDA in the reaction as detailed in the results section.

Ligand removal

$Ni_{2-x}Co_xP$ NCs dispersed in chloroform (~50 mg in 10 mL) were mixed with an equal volume fraction of 6.3 wt% hexafluorophosphoric acid (HPF_6) in formamide solution to form a two phase system. The mixture was vigorously stirred at room temperature. The final formamide solution containing the NCs was washed several times with chloroform to remove all the remaining organic ligands surrounding the NCs. The precipitate was collected after drying at room temperature for later application.

Characterization

Transmission electron microscopy (TEM) characterization was carried out using a ZEISS LIBRA 120, operating at 120 kV and a JEOL 1011 operating at 100kV. Carbon-coated TEM grids from Ted-Pella were used as substrates. High-resolution TEM (HRTEM) studies were conducted using a field emission gun FEI Tecnai F20 microscope at 200 kV with a point-to-point resolution of 0.19 nm. High angle annular dark-field (HAADF) STEM was combined with electron energy loss spectroscopy (EELS) in the Tecnai F20, by using a GATAN QUANTUM filter. Scanning electron microscopy (SEM) analyses were carried out using a ZEISS Auriga microscope with an energy dispersive X-ray spectroscopy (EDS) detector operating at 20 kV. Powder X-ray diffraction (XRD) patterns were collected directly from the as-synthesized NCs dropped on Si (501) substrate using a Bruker-AXS D8 Advanced X-ray diffractometer with Ni-filtered (2 μm thickness) Cu K radiation (λ = 1.5406 Å) operating at 40 kV and 40 mA. A LynxEye linear position-sensitive detector was used in reflection geometry. X-ray photoelectron spectroscopy (XPS) was carried out on a SPECS system equipped with an Al anode XR50 source operating at 150 mW and a Phoibos 150 MCD-9 detector. The pressure in the analysis chamber was below 10^{-7} Pa. The area analyzed was about 2 mm × 2 mm. The pass energy of the hemispherical analyzer was set at 25 eV and the energy step was set at 0.1 eV. Data processing was performed with the CasaXPS program (Casa Software Ltd., UK). Binding energy values were corrected using the C 1s peak at 284.8 eV. Fourier transform infrared spectroscopy (FTIR) was performed on an Alpha Bruker FTIR spectroscopy with a platinum attenuated total reflectance (ATR) single reflection module.

Electrochemical measurements

The catalyst ink for electrochemical measurements was prepared by mixing 5 mg of $Ni_{2-x}Co_xP$ NCs, 5 mg of carbon powder (Vulcan XC-72), 2 mL of deionized water/isopropanol (v/v = 1:1) and 35 μL of 5 wt% of Nafion solution. The mixture was sonicated for 30 min to form a homogeneous catalyst ink. A glassy carbon electrode (GCE, 5 mm in diameter) was polished using diamond paper and 0.05 μm alumina slurry sequentially, followed by ultrasonication in ethanol and water for 1 min. The cleaned GCE was dried under argon flow at room temperature. Onto the GCE, 10 μL of catalyst ink were drop casted and then dried at room temperature.

Electrochemical measurements were conducted at room temperature on a BioLogic Electrochemical workstation in a standard three-electrode cell using a modified GCE as working electrode, Pt mesh as counter electrode and Ag/AgCl as reference electrode. The HER polarization curves were obtained in 0.5 M H_2SO_4 electrolyte, which was degassed by bubbling hydrogen for 30 min before measurement. The HER

polarization curves were tested from 0 to -0.7 V versus Ag/AgCl at a scan rate of 5 mV s^{-1}. The time dependency of catalytic currents during electrolysis for NiCoP NCs was tested in 0.5 M H_2SO_4 at η = 150 mV under stirring to remove the generated gas bubbles.

DFT modeling

The density functional calculations were conducted by using the Vienna ab initio simulation package (VASP),[35,36] we selected the Projector augmented wave method (PAW) to describe the interaction between the atomic cores and electrons, with a kinetic cut-off of 300 eV.[37] The generalized gradient approximation (GGA) with the Perdew-Burke-Ernzerhof (PBE) exchange-correlation functional was applied.[38] The $Ni_{2-x}Co_xP$(200) surfaces were modeled by supercell slab containing four (0001) atomic layers to eliminate the polarity with a vacuum gap of ~15 Å. A Monkhorst-Pack grid of size of 6×6×1 was used to sample the surface Brillouin zone. The lowest two layers were fixed and the other layers were fully relaxed. The convergence criterion for total energies was set to 10^{-6} eV, simultaneously residual force were converged to 0.01 eV $Å^{-1}$ during relaxation. All bulk and slab structure of $Ni_{2-x}Co_xP$ crystals are presented in **Figures S1** and **S2** (supporting information, SI). The differential adsorption energy ΔEH can be calculated by using the equation:

$$\Delta E_H = E(Ni_{2-x}Co_xP + H^*) - E(Ni_{2-x}Co_xP) - 1/2\ E(H_2)$$

where $E(Ni_{2-x}Co_xP + H^*)$ represents the total energy of $Ni_{2-x}Co_xP$ with H atom adsorbed on surfaces, $E(Ni_{2-x}Co_xP)$ is the total energy of $Ni_{2-x}Co_xP$ slabs, and $E(H_2)$ is the energy of a hydrogen molecule in gas phase. $Ni_{2-x}Co_xP$ structures with an adsorbed H atom are presented in Figure S2. Our calculations showed that H atom would always be absorbed on the same active site of the (0001) surface of $Ni_{2-x}Co_xP$, that is on the hollow site where the H atom bonds with three metal atoms.

ΔE_H does not include the contributions from the vibrational motion and the entropy. The Gibbs free energy for hydrogen adsorption can be calculated with the equation including these corrections:

$$\Delta G_{H^*} = \Delta E_H + \Delta E_{ZPE} + \Delta_{0\rightarrow 298.15K}\Delta H_H - T\Delta S_H$$

where the ΔE_{ZPE} represents the zero point correction between adsorbed hydrogen and hydrogen in gas phase, which can be obtained from frequency calculation, the $\Delta_{0\rightarrow 298.15K}\Delta H_H$ means enthalpy change from 0 K to 298.15 K which approaches to half of $\Delta_{0\rightarrow 298.15K}\Delta H_{H2}$, and the $T\Delta S_H$ means the entropy changes from H* to H_2 in gas phase, which is approximately equivalent to 1/2 $T\Delta S_{H2}$.[39,40] Detail data are presented in **Table S1**.

Results and discussion

$Ni_{2-x}Co_xP$ ($0 \leqslant x \leqslant 2$) NCs were produced from the reaction in solution of nickel and cobalt chlorides with TPP in the presence of HDA (see experimental section for details). Composition was tuned by simply adjusting the ratio of nickel and cobalt chlorides in the precursor solution. **Figure 1** displays representative TEM micrographs of the $Ni_{2-x}Co_xP$ NCs produced following this procedure. Spherical NCs were obtained for $Ni_{2-x}Co_xP$ NCs with $x \leqslant 1.0$ and elongated NCs or nanorods for $x \geqslant 1.2$. The NC size and aspect ratio increased when increasing the amount of Co. **Table 1** displays the nominal composition and the experimental metal ratios measured by SEM-EDX. Notice that the final NC composition correlated well with the nominal metal ratios introduced.

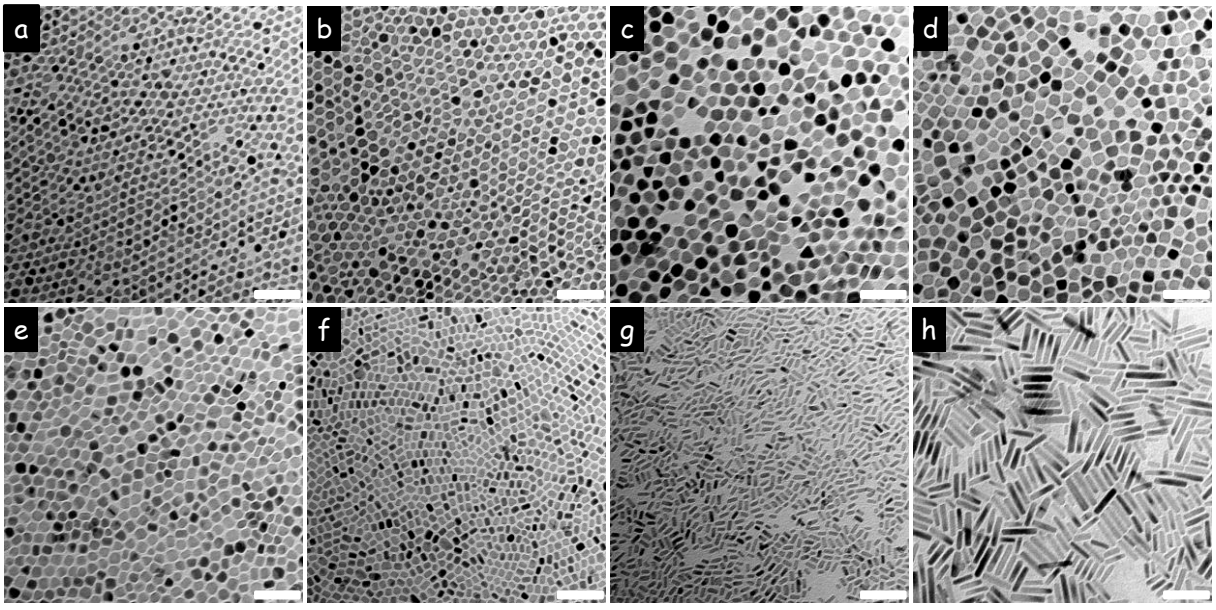

Figure 1. TEM images of $Ni_{2-x}Co_xP$ NCs with different compositions: x = 0 (a), 0.2 (b), 0.6 (c), 1 (d), 1.2 (e), 1.4 (f), 1.8 (g), 2 (h). Scale bars = 50 nm.

Table 1. Ni:Co metal ratios (nominal and EDX) and average NC size (TEM) of $Ni_{2-x}Co_xP$ NCs.

Ni:Co ratio		Average size (nm)	
Nominal	EDX	Length	Width
2.00:0.00	2.00:0.00	7.6±0.8	
1.80:0.20	1.81:0.19	9±1	
1.00:1.00	1.03:0.97	12±2	
0.80:1.20	0.82:1.18	11±1	7±1
0.60:1.40	0.54:1.46	9.0±0.7	5.3±0.6
0.20:1.80	0.17:1.83	10±1	3.6±0.7
0.00:2.00	0.00:2.00	33±6	6±1

Ni_2P and Co_2P share the same hexagonal crystal phase (P62m space group) and have similar lattice parameters. Thus, taking into account the small size of the crystal domains, $Ni_{2-x}Co_xP$ NCs with different compositions displayed very similar XRD patterns (**Figure 2**). However as the amount of Ni decreased, NCs crystallinity decreased.

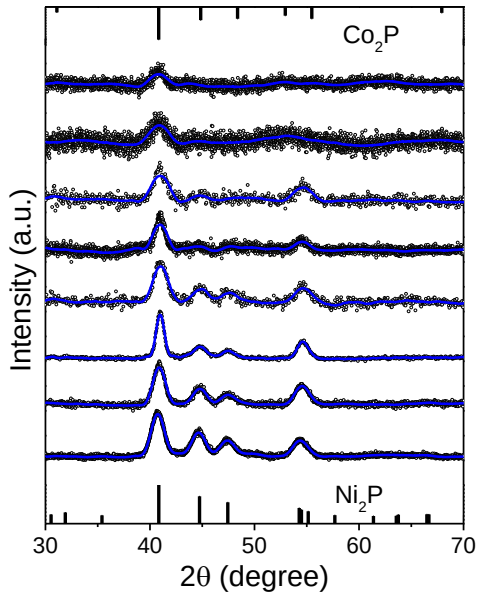

Figure 2. XRD patterns of $Ni_{2-x}Co_xP$ NCs. From bottom to top: x = 0, 0.2, 0.6, 1.0, 1.2, 1.4, 1.8, 2. Reference patterns of Ni_2P (PDF #65-9706) and Co_2P (PDF #54-0413) are also displayed at the bottom and top of the graph, respectively.

HRTEM micrographs of NiCoP (**Figure 3**) and $Ni_{0.4}Co_{1.6}P$ (**Figures S4** and **S5**) NCs confirmed their hexagonal phase and demonstrated the NCs to be single crystals. A slight decrease of the unit cell volume from NiCoP (a = b = 5.834 Å and c = 3.353 Å) to $Ni_{0.4}Co_{1.6}P$ (a = b = 5.795 Å and c = 3.371 Å) was detected by HRTEM. This small variation of the unit cell volume was consistent with the increased amount of Co, which has a slightly larger ionic radius than Ni. EELS compositional maps (**Figures 3d**, **S6** and **S8**) showed the two metals, Ni and Co, and also P to be homogeneously distributed within each NC, although a slight excess of Co was detected at the NCs surface and a small excess of Ni was measured within the NCs core (**Figure 3e**). All NCs analyzed had similar metal ratios and no binary NC could be detected after extensive EELS characterization in ternary phosphide samples (**Figures S7-S9**).

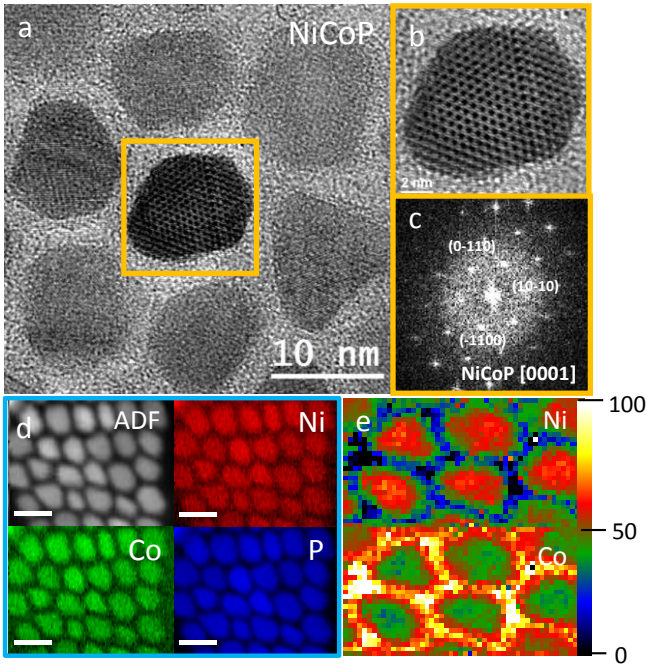

Figure 3. HRTEM micrograph of NiCoP NCs (a), detail of the NC in orange (b) and its corresponding power spectrum (c). STEM-EELS elemental composition maps (d) and quantification maps (e) of NiCoP NCs.

XPS analysis (**Figures 4** and **S10**) of the Ni $2p_{3/2}$ region of NiCoP NCs showed Ni to be present at the NC surface in two different chemical states, which we associated to NiP (852.9 eV) and a Ni^{2+} or Ni^{3+} chemical environment (856.7 eV).[41-45] An additional satellite peak was also observed at 862.2 eV.[46] The ratio between the two nickel chemical states was: $Ni^{2+/3+}$/NiP = 1.45. The Co $2p_{3/2}$ spectrum was fitted with four peaks associated to CoP (778.2 eV), a Co^{2+} chemical environmental (781.7 eV), and two satellite peaks (785.6 eV and 788.0 eV).[47,48] The amount of Co^{2+} was three times larger than that of CoP: Co^{2+}/CoP = 3.05. Two phosphorous chemical states were identified from the XPS analysis of the P 2p electronic states. A P $2p_{3/2}$ peak at 129.5 eV matched with the binding energy expected from P in a metal phosphide environment, thus we related it to P within the NiCoP structure.[46,47] A second P $2p_{3/2}$ peak at higher binding energy, 133.1 eV, was assigned to a phosphate environment.[46,49] The ratio between the two phosphorous chemical states was MP/PO = 1.02. From the XPS analysis, we conclude that the NC surface, the outermost 1-2 nm, was oxidized to a $NiCoPO_x$, while below this surface layer the chemical environment of Ni, Co and P corresponded to that of a NiCoP with a slight sharing of electrons from Ni and Co, showing electronic states with higher binding energies than the metal, to P, which showed lower binding energies than zero-valent P.

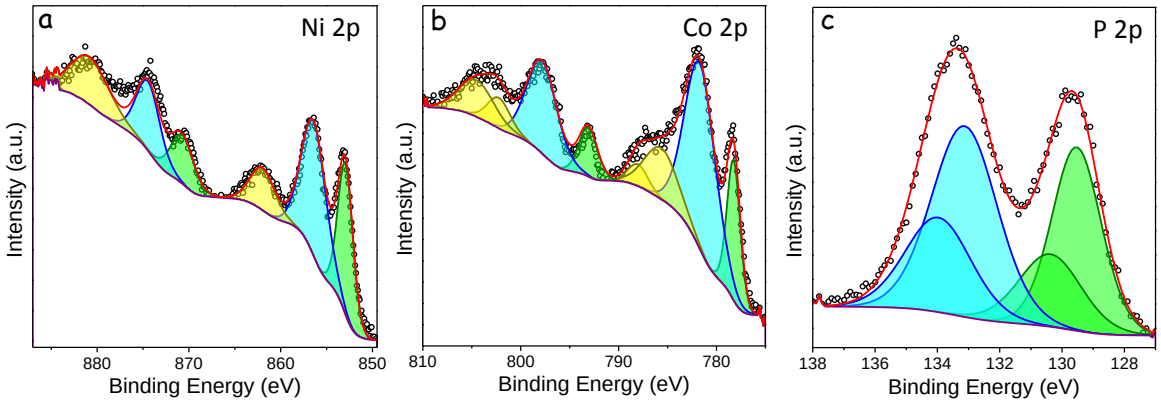

Figure 4. XPS spectra of NiCoP NCs in the Ni 2p (a), Co 2p (b) and P 2p (c) regions.

In terms of stoichiometry, XPS analysis showed a clear excess of phosphorous at the NC surface: P/(Ni+Co) = 2.9. This excess of P might be related to the presence of TPP as surface ligand and to the stripping of metal ions from the NC surface during the purification procedure [33]. The metal ratio obtained from XPS analysis showed a slight excess of cobalt, Ni/Co = 0.9, which was consistent with the EELS compositional maps showing an excess of Co at the NC surface. This slight surface segregation of Co was also consistent with the higher ratio Co^{2+}/CoP measured, when compared with $Ni^{2+/3+}$/NiP, and it could have been generated by the surface oxidation itself, owing to the slightly lower electronegativity of Co than Ni, and thus its higher affinity to oxygen.

To study the mechanism of formation of the $Ni_{2-x}Co_xP$ NCs, we analyzed aliquots of a reacting mixture at different reaction temperatures and times (**Figure 5**). We selected the NiCoP composition for this study. From the first solid product recovered, at 230 °C, only Ni and P were detected by EDX. The XRD pattern of these initial NCs displayed a weak and broad peak at ca. 62°, indicating a close to amorphous atomic structure. As the reaction temperature increased to 260 °C, Co was introduced within the NCs and the Co/Ni ratio increased to ca. Co/Ni = 0.46. The XRD pattern of the material produced at 260 °C showed a broad reflection at around 61°. Additionally a small peak at ca. 40°, around the position of the main XRD peak of the hexagonal phase of NiCoP, started to appear, demonstrating the formation of a crystalline lattice with the proper phase. By the time when the solution reached the set reaction temperature, 290 °C, the ratio of Co/Ni had increased to Co/Ni = 0.67. At this point, the broad XRD peak had shifted to about 51°, while the peak corresponding to the (111) reflection of NiCoP had become much more intense. As the reaction time increased, with the solution at 290 °C, more cobalt was introduced into the lattice, up to a final Co/Ni = 0.94 for this particular sample. Meanwhile, NCs crystallinity continuously improved (**Figure 5**). It should be pointed out that Ni_2P and Co_2P hexagonal phases display two different metal coordination sites, the tetrahedral geometry (M1) site and the square pyramidal geometry (M2) site (**Figure S11**). The square pyramidal geometry site is larger than the tetrahedral site.[50] Therefore, in a NiCoP crystal, the slightly larger Co^{2+} ions are expected to occupy the larger M2 site, while slightly smaller Ni^{2+} ions would occupy the M1 sites.[51]

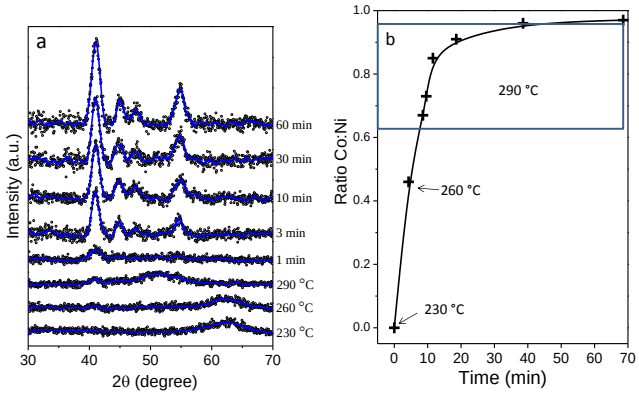

Figure 5. a) XRD patterns obtained from aliquots extracted from a NiCoP NCs reaction mixture at different temperatures and reaction times. b) Ratio of the Co and Ni composition, Co/Ni, in the solid products precipitated from aliquots, as measured by EDX.

To analyze the influence of TPP and HDA on the $Ni_{2-x}Co_xP$ NCs size and geometry, NCs were grown from solutions containing different amounts of these compounds. **Figure 6** shows the TEM images, size distribution histograms and XRD patterns of the NiCoP NCs obtained from the reaction of 1 mmol of metal chlorides with different amounts of TPP, from 3 to 20 mmol. As the amount of TPP increased, the average size of the obtained NiCoP NCs increased from 8 ± 1 to 24 ± 3 nm. We believe that TPP plays a double role in the formation of the precursor metal complexes: as phosphorous source and as reducing agent. It is through this second role that it controls the NCs size. As the amount of TPP increases, a faster growth rate is obtained during the first stage of the synthesis, thus the free monomer concentration is more rapidly reduced, limiting the number of nucleation events, thus the number of NCs formed, and thus resulting in larger NCs.[52]

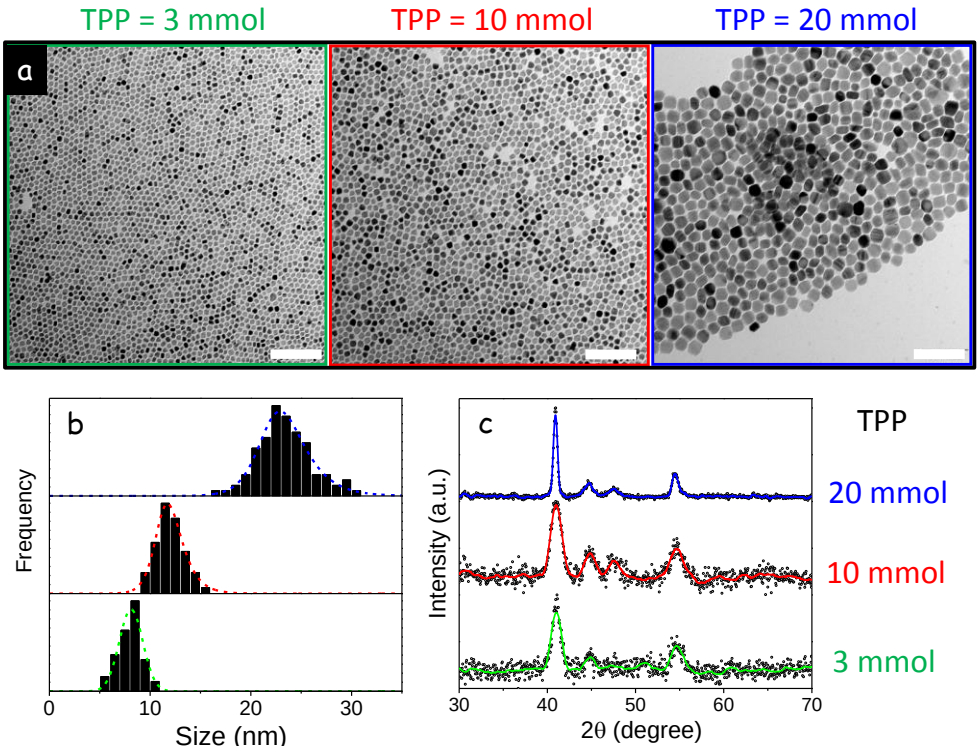

Figure 6. Representative TEM micrographs (a), size distribution histograms (b) and XRD patterns (c) of NiCoP NCs produced using 1 mmol of metals and 3 mmol, 10 mmol or 20 mmol of TPP, as indicated. Scale bars = 100 nm.

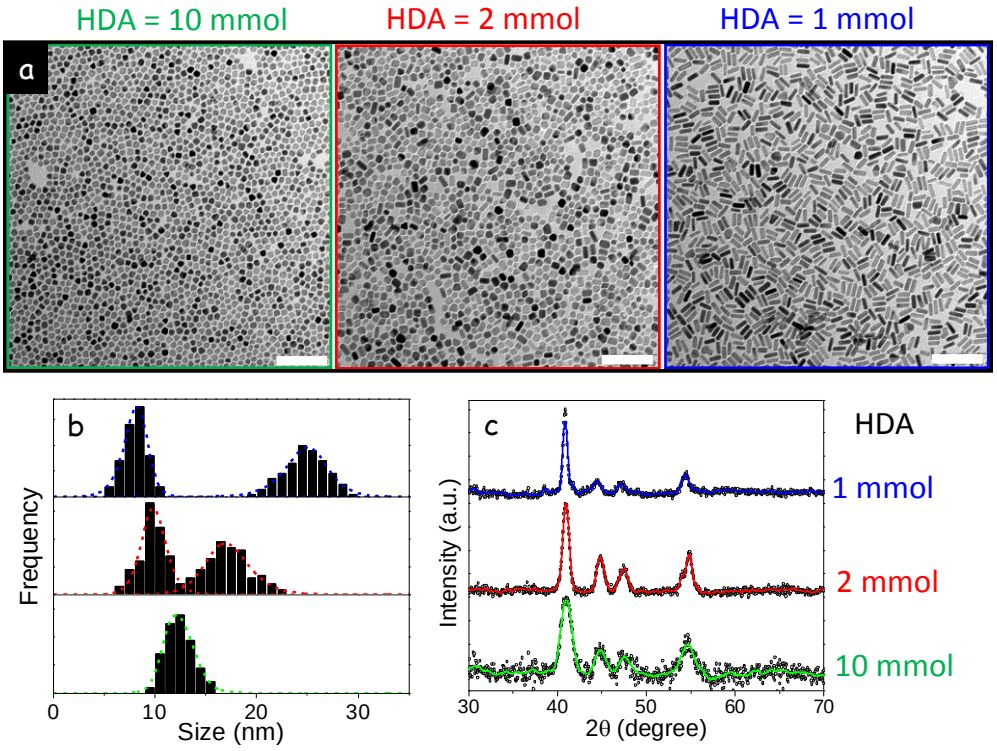

Figure 7. Representative TEM micrographs (a), size distribution histograms, including width and length for the elongated NCs (b) and XRD patterns (c) of NiCoP NCs produced from the reaction of 1 mmol of metals in the presence of 10 mmol, 2 mmol and 1 mmol of HDA. Scale bars = 100 nm.

Figure 7 shows TEM images, size distribution histograms and XRD patterns of NiCoP NCs obtained from the reaction of the 1 mmol of metal chlorides with 10 mmol TPP, in the presence of different amounts of HDA, from 10 mmol to 1 mmol. With excess amounts of HDA, quasi spherical NiCoP NCs were formed. However, as the amount of HDA was reduced, the NiCoP NCs morphology became elongated, and at equivalent metal and HDA concentrations, NiCoP nanorods were produced. We observed the presence of HDA to be essential for the metal chlorides to be dissolved in the ODE solution. HDA probably reacts with the metal ions to form a complex, promoting in this way the precursor dissolution. We also experimentally observed the dissolution of the cobalt chloride to require lower amounts of HDA compared with nickel chloride, and that the reactivity of the formed cobalt monomer was lower than that of the nickel, as cobalt incorporated at higher reaction temperature to the growing $Ni_{2-x}Co_xP$ NCs. Additionally, HDA binds at the surface of $Ni_{2-x}Co_xP$ NCs influencing their growth and rendering them colloidally stable in non-polar solvent. On the other hand, using cobalt(II) and nickel(II) chlorides as metal precursors, two-fold larger amounts of chlorine ions than metal ions were present in solution. We initially hypothesized that chlorine ions could play a strong role on directing the asymmetric growth of the NCs. Such an effect of chlorine ions was previously reported for CdSe NCs for example.[53,54] When present in relatively high concentration compared with HDA, chlorine could preferentially bind at particular $Ni_{2-x}Co_xP$ NC facets controlling the final NC shape. However, we produced Co_2P NCs using the exact same protocol as detailed above, but using cobalt(II) nitrate instead of chloride as cobalt precursor. With no chlorine in solution, we also obtained Co_2P nanorods (**Figure S12**). Thus, we had to discard a role of chlorine on the geometry control of the NCs. Taking into account the collected experimental evidences, we conclude that HDA itself preferentially binds to specific $Ni_{2-x}Co_xP$ NC facets. When moderate amounts of HDA are present in solution, this preferential binding translates into the growth of asymmetric NCs. However, when excess amounts of this molecule are introduced in the reaction mixture, a homogenous HDA coverage throughout the whole surface is obtained, resulting in spherical NCs. Because cobalt interacts more strongly than Ni with HDA, the influence of this surface ligand on the control of the growth of cobalt-rich NCs is also more severe than in nickel-rich, what explains that we can obtain more elongated NCs the higher the cobalt content at a set HDA concentration. XRD patterns showed the increase of the relative intensity of the (111) reflection with the nanorods formation, confirming this one to be the preferential growth direction.

The synthetic protocol proposed here was characterized by an excellent reproducibility and production yields above 90% after purification. The two types of precursor used, metal chlorides and TPP, are relatively low cost, are stable in ambient conditions and present a low-toxicity. The synthetic protocol was designed to make use of a heating up strategy to facilitate up scaling. We explored the scale up of the present synthetic procedure to the production of $Ni_{2-x}Co_xP$ NCs at the gram scale. We simply increased a factor 20 the amounts of metal chlorides, TPP and HDA, but increased just a factor 10 the volume of solvent, ODE, thus raising a two-fold the concentration. We also prolonged both the initial solvent cleaning step and the reaction time to 2 h. The $Ni_{2-x}Co_xP$ NCs produced from this straightforward scaling up showed an excellent quality with very narrow size distributions, a high reproducibility and above 90% yields (**Figure 8**).

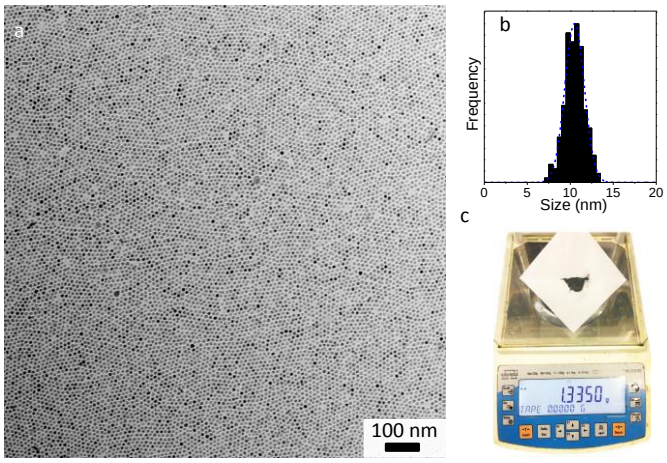

Figure 8. a) Representative TEM micrograph and b) size distribution histogram of the NiCoP NCs produced in a scaled up procedure resulting in over 1 g of NCs per batch (c).

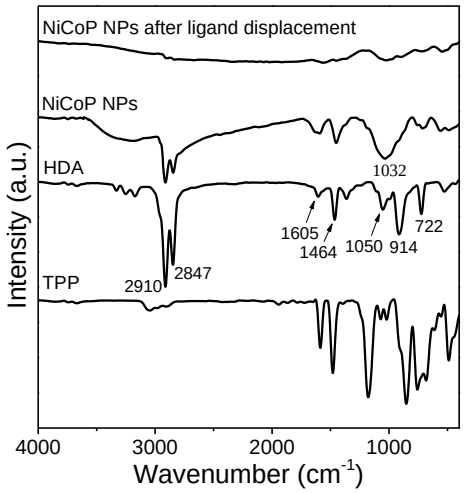

Figure 9. FTIR of TPP, HDA, NiCoP NCs before and after ligand removal.

FTIR spectra were consistent with the presence of HDA ligands at the $Ni_{2-x}Co_xP$ NC surface (**Figure 9**). FTIR peaks at 2910 and 2847 cm^{-1} were attributed to C-H stretching vibrations of alkyl groups from HDA. The peaks at 1464 and 722 cm^{-1} were assigned to C-H bending vibrations and the peak at 1605 cm^{-1} corresponded to the N-H bending vibration. For free HDA, two clear peaks at 1050 and 914 cm^{-1} were assigned to the C-N and C-C stretching vibration, respectively. However, those peaks appeared merged in a broad band centered at 1032 cm^{-1} in the FTIR spectrum from the $Ni_{2-x}Co_xP$ NCs. Organic

ligands were stripped from the $Ni_{2-x}Co_xP$ NCs surface through mixing them with HPF_6 in formamide solution to form a two phase system that was vigorously stirred at room temperature. The absence of stretching modes of C-H, C-C and C-N in the final $Ni_{2-x}Co_xP$ NCs confirmed the elimination of HDA from the NC surface.

The electrocatalytic activity of $Ni_{2-x}Co_xP$ NCs with different composition was tested toward the HER in acidic conditions. Electrodes were prepared by drop casting an ink prepared by mixing $Ni_{2-x}Co_xP$ NCs with carbon powder and Nafion onto a GCE (see experimental section for details). Electrochemical measurements were conducted at room temperature in a standard three-electrode cell using the $Ni_{2-x}Co_xP$ NC-based catalyst as working electrode, a Pt mesh as counter electrode and Ag/AgCl as reference electrode. The HER polarization curves were obtained in H_2-saturated 0.5 M H_2SO_4 aqueous solutions. **Figure 10a** shows linear sweep voltammograms (LSVs) of the electrodes produced from $Ni_{2-x}Co_xP$ NCs with different compositions. Data for the GCE and a commercial Pt/C electrocatalysts was also plotted as a reference. **Figure 10b** shows the overpotential at J = 10 mA cm^{-2} as a function of the composition. As expected, the Pt/C catalyst showed an excellent HER performance with a very low overpotential, while the bare GCE showed negligible HER activity. Binary Ni_2P exhibited HER activity with an overpotential of 136 mV at J = 10 mA cm^{-2}. As cobalt was introduced within ternary $Ni_{2-x}Co_xP$ NCs, improved performances were obtained and the overpotential at J = 10 mA cm^{-2} decreased down to 97 mV for NiCoP NCs. When increasing the amount of Co above the Co:Ni = 1:1 metal ratio, worse electrocatalytic properties were again measured until an overpotential of 118 mV for Co_2P. Notice that the overpotential of the electrode based on NiCoP NCs was lower than that obtained from most other non-noble metal-based electrocatalysts reported for HER in acid media, including MoS_2, $CoSe_2$, WS_2, Ni_3S_2, Co_2P, FeP, $WS_{2(1-x)}P_{2x}$ and $CoMoS_3$ (**Table S2** and **S3**).

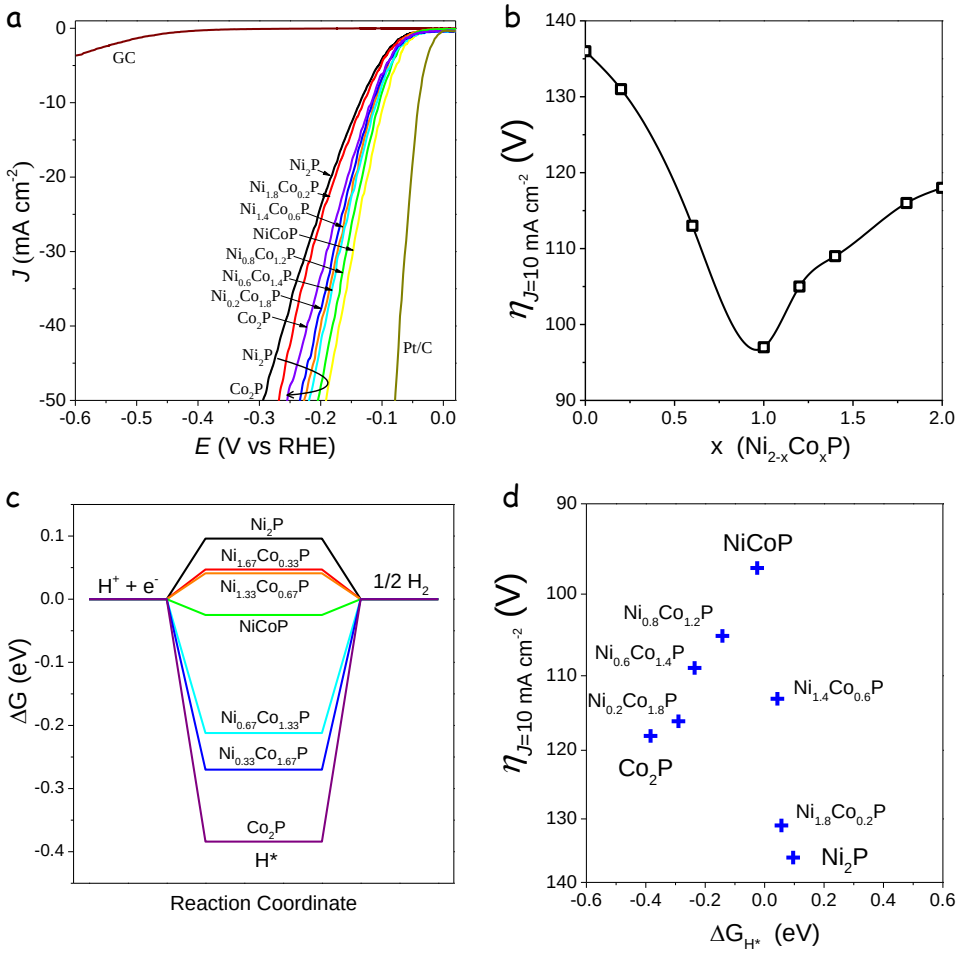

Figure 10. a) Polarization curves of GCE, $Ni_{2-x}Co_xP$ and Pt/C in 0.5 M H_2SO_4 solution. b) Overpotential at 10 mA cm^{-2} as a function of composition for the different $Ni_{2-x}Co_xP$ electrocatalysts. c) Free-energy diagram for atomic hydrogen adsorption on the $Ni_{2-x}Co_xP$ (0001) surface. d) Overpotential at 10 mA cm^{-2} as a function of the Gibbs free energy for atomic hydrogen adsorption at the $Ni_{2-x}Co_xP$ surface.

To understand the variation of catalytic activity with the composition, we investigated the HER pathways on $Ni_{2-x}Co_xP$ catalysts by DFT calculations. A series of $Ni_{2-x}Co_xP$ (x = 0, 0.33, 0.67,1, 1.33, 1.67, 2) crystals were created with the hexagonal crystal phase (**Figure S1**). The HER pathway is generally depicted as a three-state diagram, with an initial state of $H^+ + e$, an intermediate adsorbed H*, being * the adsorption site, and a final product of $1/2H_2$ in acidic media.[55,56] The lower the Gibbs free energy of the adsorbed atomic hydrogen, ΔG_{H^*}, the stronger the bond between this adsorbed hydrogen and the catalyst. Materials that bind hydrogen atoms too strongly, do not allow the hydrogen release thus blocking active sites and failing to efficiently evolve hydrogen. On the other hand, materials that bind hydrogen too weakly, hinder the step of proton/electron-transfer because they fail to stabilize the intermediate state, thus also prevent an efficient HER to take place.[40] ΔG_{H^*} is thus a reasonable descriptor to evaluate the HER activity of catalysts Taking into account this unique descriptor, the Sabatier principle predicts a volcano distribution of the catalyst performance as a function of ΔG_{H^*}, peaking at $\Delta G_{H^*} = 0$.

To deep inside the observed dependence of the $Ni_{2-x}Co_xP$ catalysts performance toward HER, we calculated ΔG_{H^*} on the most active (0001) surface of $Ni_{2-x}Co_xP$ crystals. **Figure 10c** shows the relationship between the value of ΔG_{H^*} and Co content, indicating that the value of ΔG_{H^*} decreased with Co content increasing. When the percentage of Co was 50% (NiCoP), the value of ΔG_{H^*} is -0.025eV, which is the minimum $|\Delta G_{H^*}|$ value among all the $Ni_{2-x}Co_xP$ compositions tested (calculation details are given in **Table S1**). This result is consistent with the experimental results showing the NiCoP catalysts to have the highest activity toward HER among the $Ni_{2-x}Co_xP$ series measured.

We observed that the DFT calculated ΔG_{H^*} rapidly separated from the optimum value when increasing the cobalt concentration above x = 1, while the ΔG_{H^*} variation in the Ni rich side was not so abrupt. This result does not match with the moderate performance change obtained when moving from NiCoP to Co_2P, if compared with the stronger loss of performance measured when moving from NiCoP to Ni_2P. Therefore, additional parameters, beyond ΔG_{H^*}, need to be considered to explain the compositional dependence of the $Ni_{2-x}Co_xP$ catalysts performance toward HER.

The stability of NiCoP for HER was analysed through chronoamperometric measurements. The NiCoP catalyst exhibited a high stability toward HER at about 30 mA cm^{-2} for 12 h, with a current density decrease of ca. 11% (**Figure S13**).

Conclusions

In summary, monodisperse $Ni_{2-x}Co_xP$ ($0 \leqslant x \leqslant 2$) NCs were synthesized using metal chlorides as metal precursors, TPP as phosphorus precursor and HDA as ligand. Different compositions, sizes and morphologies could be prepared simply by tuning the ratio of metal chlorides, TPP and HDA, respectively. The synthetic approach was up-scaled to the production of $Ni_{2-x}Co_xP$ at the gram scale with yields above 90%. $Ni_{2-x}Co_xP$ NCs, mixed with carbon black and Nafion, showed notable HER activities. In particular, NiCoP electrocatalysts showed best performances with an overpotential of 97 mV at 10 mA cm^{-2}, and significant long-term stability. The dependence of the catalyst performance with the composition qualitatively matched the variation of the Gibbs free energy for atomic hydrogen adsorption at the $Ni_{2-x}Co_xP$ surface. Ni-rich compositions were characterized by too low adsorption energies that were not effective for proton reduction, while Co-rich NCs showed too high binding energies that limited hydrogen desorption, thus blocking adsorption sites. This low-cost and straightforward synthesis method for $Ni_{2-x}Co_xP$ NCs showed potential application for industrial production of catalysts for HER. Furthermore, such a synthetic protocol is expected to be expanded as a general strategy for other multinary metal phosphides.

Conflicts of interest

There are no conflicts of interest to declare.

Acknowledgements

J. David and J. Arbiol acknowledge funding from Generalitat de Catalunya 2017 SGR 327 and the Spanish MINECO project VALPEC (ENE2017-85087-C3). ICN2 acknowledges support from the Severo Ochoa Programme (SEV-2013-0295) and is funded by the CERCA Programme / Generalitat de Catalunya. J. David has received funding from the European Union's Horizon 2020 research and innovation programme under the Marie Sklodowska-Curie grant agreement No 665919. J. Llorca is a Serra Hunter Fellow and is grateful to ICREA Academia program and grants MINECO/FEDER ENE2015-63969-R and GC 2017 SGR 128. J. Liu, J. Li and X. Yu thank the China Scholarship Council for scholarship support. M. Meyns acknowledges a Juan de la Cierva formación grant by the Spanish MINECO.

Notes and references

1 Y. Shi, B. Zhang, *Chem. Soc. Rev.* 2016, **45**, 1529-1541.
2 Y. Shao, X. Shi, H. Pan, *Chem. Mater.* 2017, **29**, 8892-8900.
3 J. Tian, Q. Liu, A. M. Asiri, X. Sun, *J. Am. Chem. Soc.* 2014, **136**, 7587-7590.
4 E. J. Popczun, J. R. McKone, C. G. Read, A. J. Biacchi, A. M. Wiltrout, N. S. Lewis, R. E. Schaak, *J. Am. Chem. Soc.* 2013, **135**, 9267-9270.
5 X. Wang, Y. V. Kolen'ko, X. Q. Bao, K. Kovnir, L. Liu, *Angew. Chem. Int. Ed.* 2015, **54**, 8188-8192.
6 H. Yang, Y. Zhang, F. Hu, Q. Wang, *Nano Lett.* 2015, **15**, 7616-7620.
7 D. Y. Chung, S. W. Jun, G. Yoon, H. Kim, J. M. Yoo, K. S. Lee, T. Kim, H. Shin, A. K. Sinha, S. G. Kwon, K. Kang, T. Hyeon, Y. E. Sung, *J. Am. Chem. Soc.* 2017, **139**, 6669-6674.
8 Y. Liang, Q. Liu, A .M. Asiri, X. Sun, Y. Luo, *ACS Catal.* 2014, **4**, 4065-4069.
9 Z. Xing, Q. Liu, A. M. Asiri, X. Sun, *Adv. Mater.* 2014, **26**, 5702-5707.
10 J. M. McEnaney, J. C. Crompton, J. F. Callejas, E. J. Popczun, C. G. Read, N. S. Lewis, R. E. Schaak, *Chem. Commun.* 2014, **50**, 11026-11028.

11 J. F. Callejas, C. G. Read, E. J. Popczun, J. M. McEnaney, R. E. Schaak, *Chem. Mater.* 2015, **27**, 3769-3774.
12 D. Ha, B. Han, M. Risch, L. Giordano, K. P. C. Yao, P. Karayaylali, Y. Shao-Horn, *Nano Energy* 2016, **29**, 37-45.
13 B. Zhang, Y. H. Lui, L. Zhou, X. Tang, S. Hu. *J. Mater. Chem. A* 2017, **5**, 13329-13335.
14 D. Liu, T. Liu, L. Zhang, F. Qu, G. Du, A. M. Asiri, X. Sun. *J. Mater. Chem. A* 2017, **5**, 3208-3213.
15 Y. Li, H. Zhang, M. Jiang, Q. Zhang, P. He, X. Sun, *Adv. Funct. Mater.* 2017, **27**, 1702513.
16 R. Zhang, X. Wang, S. Yu, T. Wen, X. Zhu, F. Yang, X. Sun, X. Wang, W. Hu, *Adv. Mater.* 2017, **29**, 1605502.
17 C. Tang, L. Gan, R. Zhang, W. Lu, X. Jiang, A. M. Asiri, X. Sun, J. Wang, L. Chen, *Nano Lett.* 2016, **16**, 6617-6621.
18 S. H. Ahn, A. Manthiram, *J. Mater. Chem. A* 2017, **5**, 2496-2503.
19 T. Liu, X. Ma, D. Liu, S. Hao, G. Du, Y. Ma, A. M. Asiri, X. Sun, L. Chen, *ACS Catal.* 2016, **7**, 98-102.
20 X. Wang, H. Chen, Y. Xu, J. Liao, B. Chen, H. Rao, D. Kuang, C. Su, *J. Mater. Chem. A* 2017, **5**, 7191-7199.
21 Z. Zhao, D. E. Schipper, A. P. Leitner, H. Thirumalai, J. Chen, L. Xie, F. Qin, M. K. Alam, L. C. Grabow, S. Chen, D. Wang, Z. Ren, Z. Wang, K. H. Whitmire, J. Bao, *Nano Energy* 2017, **39**, 444-453.
22 Y. Li, J. Liu, C. Chen, X. Zhang, J. Chen, *ACS Appl. Mater. Inter.* 2017, **9**, 5982-5991.
23 C. Du, L. Yang, F. Yang, G. Cheng, W. Luo, *ACS Catal.* 2017, **7**, 4131-4137.
24 J. Li, G. Wei, Y. Zhu, Y. Xi, X. Pan, Y. Ji, I. V. Zatovsky, W. Han, *J. Mater. Chem. A* 2017, **5**, 14828-14837.
25 C. Wang, J. Jiang, T. Ding, G. Chen, W. Xu, Q. Yang, *Adv. Mater. Inter.* 2016, **3**, 1500454.
26 H. Liang, A. N. Gandi, D. H. Anjum, X. Wang, *Nano Lett.* 2016, **16**, 7718-7725.
27 J. Li, M. Yan, X. Zhou, Z. Q. Huang, Z. Xia, C. R. Chang, Y. Ma, Y. Qu, *Adv. Funct. Mater.* 2016, **26**, 6785-6796.
28 Y. Bai, H. Zhang, L. Liu, H. Xu, Y. Wang, *Chemistry* 2016, **22**, 1021-1029.
29 M. Kong, Z. Wang, W. Wang, M. Ma, D. Liu, S. Hao, R. Kong, G. Du, A. M. Asiri, Y. Yao, X. Sun, *Chem-Eur. J.* 2017, **23**, 4435-4441.
30 S. Liu, C. Ma, L. Ma, Chem. *Phys. Lett.* 2015, **638**, 52-55.
31 Y. M. Hu, M. C. Liu, Y. X. Hu, Q. Q. Yang, L. B. Kong, L. Kang, *Electrochim. Acta* 2016, **215**, 114-125.
32 K. E. Marusak, A. C. Johnston-Peck, W. C. Wu, B. D. Anderson, J. B. Tracy, *Chem. Mater.* 2017, **29**, 2739-2747.
33 D. R. Liyanage, S. J. Danforth, Y. Liu, M. E. Bussell, S. L. Brock, *Chem. Mater.* 2015, **27**, 4349-4357.
34 J. Liu, M. Meyns, T. Zhang, J. Arbiol, A. Cabot, A. Shavel, *Chem. Mater.* 2018, **30**, 1799-1807.
35 G. Kresse, J. Furthmüller, *Phys. Rev. B* 1996, **54**, 11169-11186.
36 G. Kresse, J. Furthmüller, *Comp. Mater. Sci.* 1996, **6**, 15-50.
37 G. Kresse, D. Joubert, *Phys. Rev. B* 1999, **59**, 1758-1775.
38 J. P. Perdew, K. Burke, M. Ernzerhof, *Phys. Rev. Lett.* 1996, **77**, 3865-3868.
39 D. Voiry, H. Yamaguchi, J. Li, R. Silva, D. C. B. Alves, T. Fujita, M. W. Chen, T. Asefa, V. Shenoy, G. Eda, *Nat. Mater.* 2013, **12**, 850-855.
40 H. Duan, D. Li, Y. Tang, Y. He, S. Ji, R. Wang, H. Lv, P. P. Lopes, A. P. Paulikas, H. Li, S. X. Mao, C. Wang, N. M. Markovic, J. Li, V. R. Stamenkovic, Y. Li, *J. Am. Chem. Soc.* 2017, **139**, 5494–5502.
41 M. Zhi, X. Chen, H. Finklea, I. Celik, N. Q. Wu, *J. Power Sources* 2008, **183**, 485-490.
42 B. Elsener, M. Crobu, M. A. Scorciapino, A. Rossi, *J. Appl. Electrochem.* 2008, **38**, 1053-1060.
43 Z. Qi, W. Lee, Tribol. Int. 2010, **43**, 810-814.
44 P. Lo, W. Tsai, J. Lee, M. Hung, *J. Electrochem. Soc.* 1995, **142**, 91-96.
45 H. Zhang, Y. Lu, C. D. Gu, X. L. Wang, J. P. Tu, *CrystEngComm* 2012, **14**, 7942-7950.
46 J. F. Moulder, W. F. Stickle, P. E. Sobol, K. D. Bomben, Handbook of X-ray photoelectron spectroscopy, Perkin-Elmer 1992.
47 A. P. Grosvenor, S. D. Wik, R. G. Cavell, A. Mar, *Inorg. Chem.* 2005, **44**, 8988-8998.
48 P. Jiang, Q. Liu, C. Ge, W. Cui, Z. Pu, A. M. Asiri, X. Sun, *J. Mater. Chem. A* 2014, **2**, 14634-14640.
49 Z. G. Zhao, J. Zhang, Y. Yuan, H. Lv, Y. Tian, D. Wu, Q. W. Li, *Sci Rep.* 2013, **3**, 2263.
50 A. Hitihami-Mudiyanselage, M. P. Arachchige, T. Seda, G. Lawes, S. L. Brock, *Chem. Mater.* 2015, **27**, 6592-6600.
51 R. D. Shannon, *Acta Cryst.* 1976, **A32**, 751-767.
52 D. Li, M. P. Arachchige, B. Kulikowski, G. Lawes, T. Seda, S. L. Brock, *Chem. Mater.* 2016, **28**, 3920-3927.
53 M. Meyns, F. Lacono, C. Palencia, J. Geweke, M. D. Coderch, U. E. A. Fittschen, J. M. Gallego, R. Otero, B. H. Juarez, C. Klinke, *Chem. Mater.* 2014, **26**, 1813-1821.
54 C. Palencia, K. Lauwaet, L. Cueva, M. Acebron, J. J. Conde, M. Meyns, C. Klinke, J. Gallego, R. Otero, B. H. Juarez, *Nanoscale* 2014, **6**, 6812-6818.
55 J. K. Nørskov, T. Bligaard, A. Logadottir, J. Kitchin, J. G. Chen, S. Pandelov, U. Stimming, *J. Electrochem. Soc.* 2005, **152**, J23–J26.
56 H. Liang, A. N. Gandi, D. H. Anjum, X. Wang, U. Schwingenschlögl, H. N. Alshareef. *Nano Lett.* 2016, **16**, 7718–7725.

TOC graphical abstract

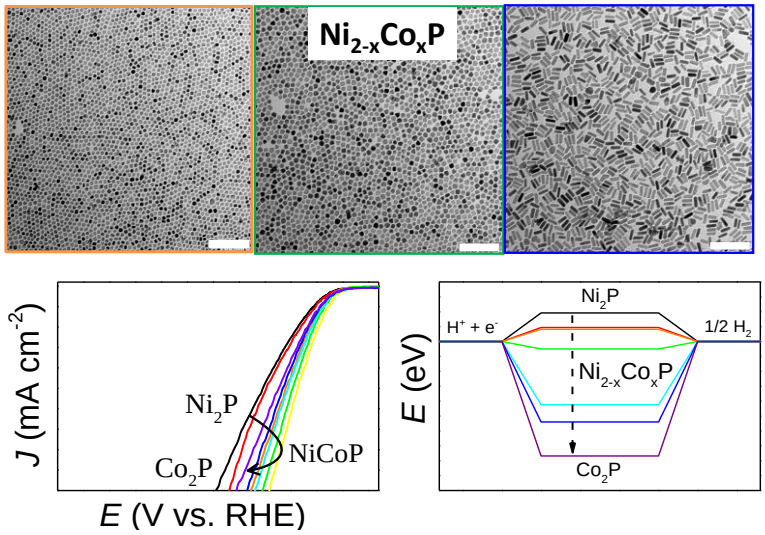

Supporting information

Colloidal $Ni_{2-x}Co_xP$ nanocrystals for the hydrogen evolution reaction

Junfeng Liu,[a] Zhenxing Wang,[b] Jeremy David,[c] Jordi Llorca,[d] Junshan Li,[a] Xiaoting Yu,[a] Alexey Shavel,[a] Jordi Arbiol,[ce] Michaela Meyns,*[a] Andreu Cabot*[ae]

[a] Catalonia Institute for Energy Research (IREC), Sant Adrià de Besòs, 08930 Barcelona, Spain

[b] State Key Laboratory of Electrical Insulation and Power Equipment, Xi'an Jiaotong University, 710049, Xi'an, China

[c] Catalan Institute of Nanoscience and Nanotechnology (ICN2), CSIC and BIST, Campus UAB, Bellaterra, 08193 Barcelona, Catalonia, Spain

[d] Institute of Energy Technologies, Department of Chemical Engineering and Barcelona Research Center in Multiscale Science and Engineering, Universitat Politecnica de Catalunya, Eduard Maristany 10-14, 08019 Barcelona, Spain

[e] ICREA, Pg. Lluis Companys 23, 08010 Barcelona, Catalonia, Spain

* Corresponding author

E-mail: michaela.meyns@awi.de, acabot@irec.cat

Contents

1. **DFT calculations**

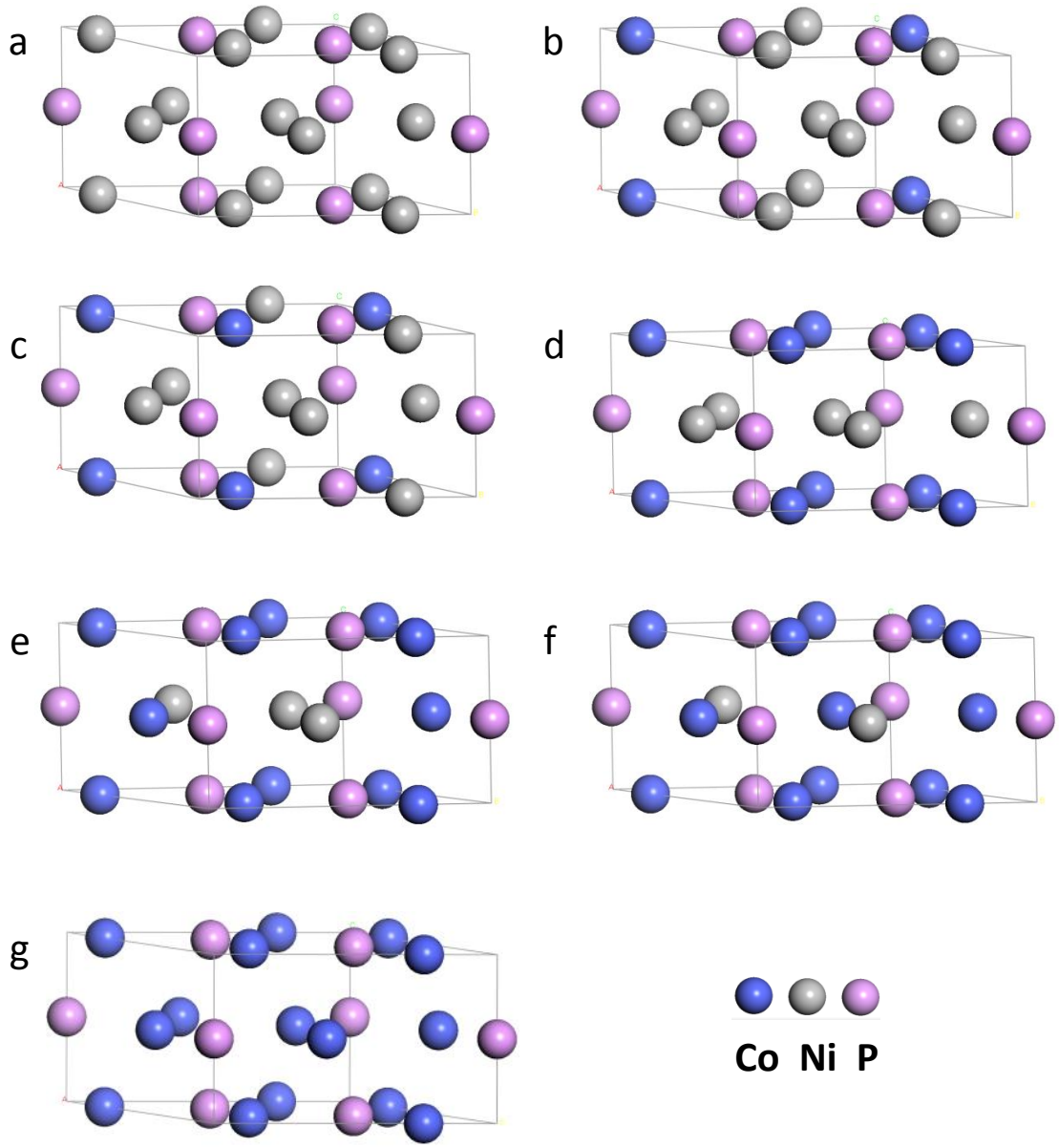

Figure S1. Hexagonal crystal structures of the $Ni_{2-x}Co_xP$: (a) Crystal structure of Ni_2P(a = b = 5.884 Å, c = 3.369 Å); (b) Crystal structure of $Ni_{1.67}Co_{0.33}P$ (a = b = 5.871Å, c = 3.338 Å); (c) Crystal structure of $Ni_{1.33}Co_{0.67}P$ (a = 5.838 Å, b = 5.849 Å, c = 3.325Å); (d) Crystal structure of NiCoP (a = b = 5.805 Å, c = 3.344 Å); (e) Crystal structure of $Ni_{0.67}Co_{1.33}P$ (a = 5.729, b = 5.893 Å, c = 3.363Å); (f) Crystal structure of $Ni_{0.33}Co_{1.67}P$ (a = 5.673 Å ,b = 5.794 Å, c = 3.389 Å); (g) Crystal structure of Co_2P (a = b = 5.725 Å, c = 3.409 Å).

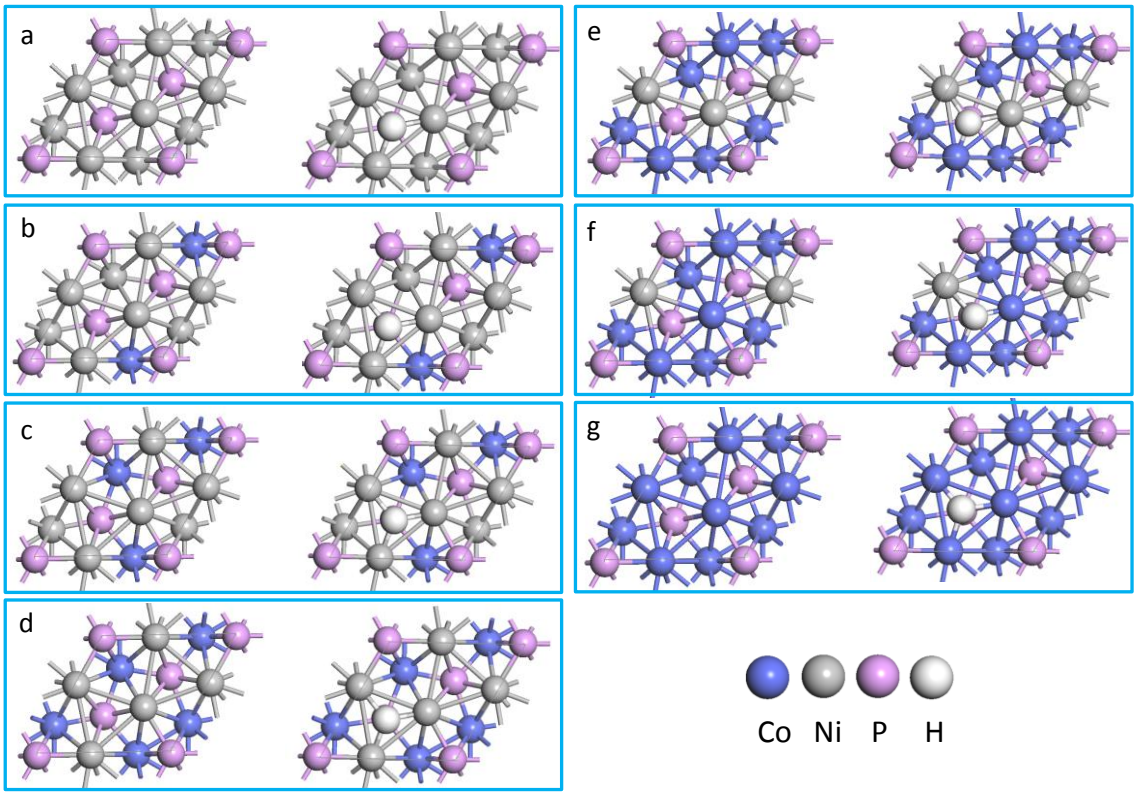

Figure S2. Top view of the (0001) surface of $Ni_{2-x}Co_xP$ (left panel) and the (0001) surface on which H*absorbed (right panel).(a) the (0001) surface of Ni_2P (d_{Ni-H} = 1.793 Å); (b) the (0001) surface of $Ni_{1.67}Co_{0.33}P$ (d_{Ni-H} = 1.801 Å); (c) the (0001) surface of $Ni_{1.33}Co_{0.67}P$ (d_{Ni-H} = 1.804 Å); (d) the (0001) surface of NiCoP (d_{Ni-H} = 1.792 Å); (e) the (0001) surface of $Ni_{0.67}Co_{1.33}P$ (d_{Ni-H} = 1.821 Å, d_{Co-H} = 1.747 Å); (f) the (0001) surface of $Ni_{0.33}Co_{1.67}P$ (d_{Ni-H} = 1.874 Å, d_{Co-H} = 1.769 Å); (g) the (0001) surface of Co_2P(d_{Co-H} = 1.801 Å).

Table S1. Calculated adsorption energies and Gibbs free energies of H adsorption on $Ni_{2-x}Co_xP$ (0001) surface.

Composition	ΔE_H (eV)	ΔE_{ZPE} (eV)	$\Delta_{0\rightarrow298.15K}\Delta H_H$ (eV)	$-T\Delta S_H$ (eV)	ΔG_{H^*} (eV)
Ni_2P	-0.228	0.067	0.052	0.205	0.096
$Ni_{1.67}Co_{0.33}P$	-0.196	-0.014	0.052	0.205	0.047
$Ni_{1.33}Co_{0.67}P$	-0.211	-0.005	0.052	0.205	0.041
NiCoP	-0.325	0.043	0.052	0.205	-0.025
$Ni_{0.67}Co_{1.33}P$	-0.508	0.039	0.052	0.205	-0.212
$Ni_{0.33}Co_{1.33}P$	-0.565	0.038	0.052	0.205	-0.270
Co_2P	-0.699	0.058	0.052	0.205	-0.384

2. Size distribution

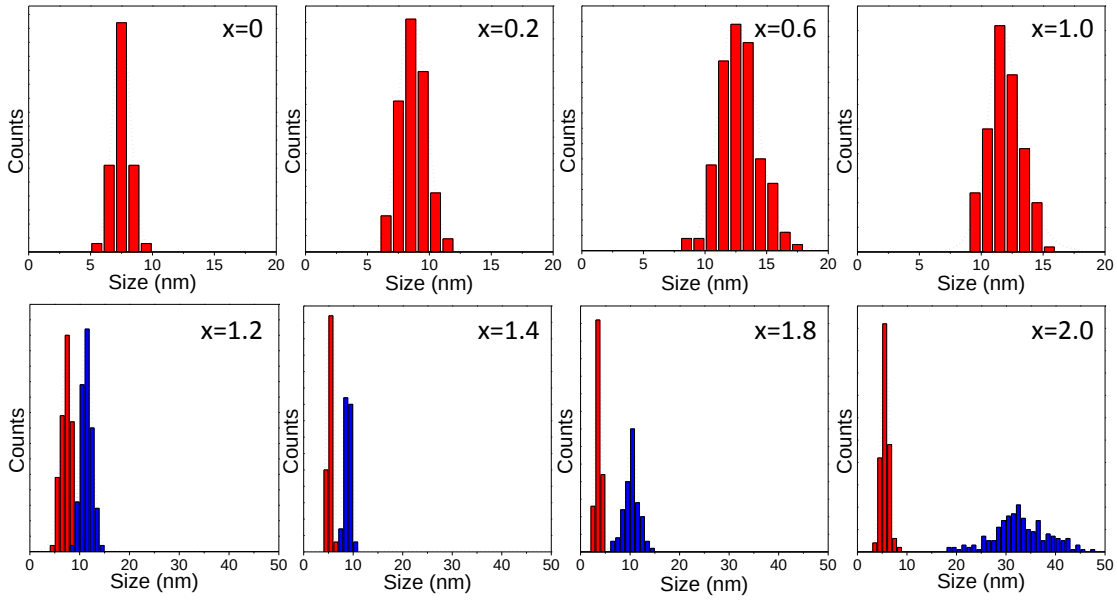

Figure S3. Size distributions of $Ni_{2-x}Co_xP$ (x=0, 0.2, 0.6, 1.0, 1.2, 1.4, 1.8 and 2.0) NPs.

3. Additional HRTEM characterization

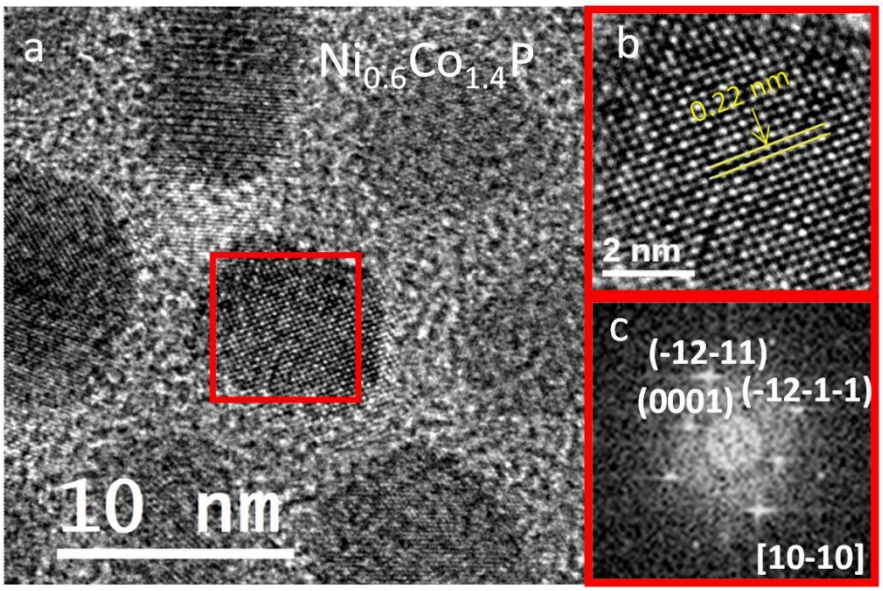

Figure S4. HRTEM micrograph of $Ni_{0.6}Co_{1.4}P$ NPs (a), detail of the NP in red (b) and its corresponding power spectrum (c).

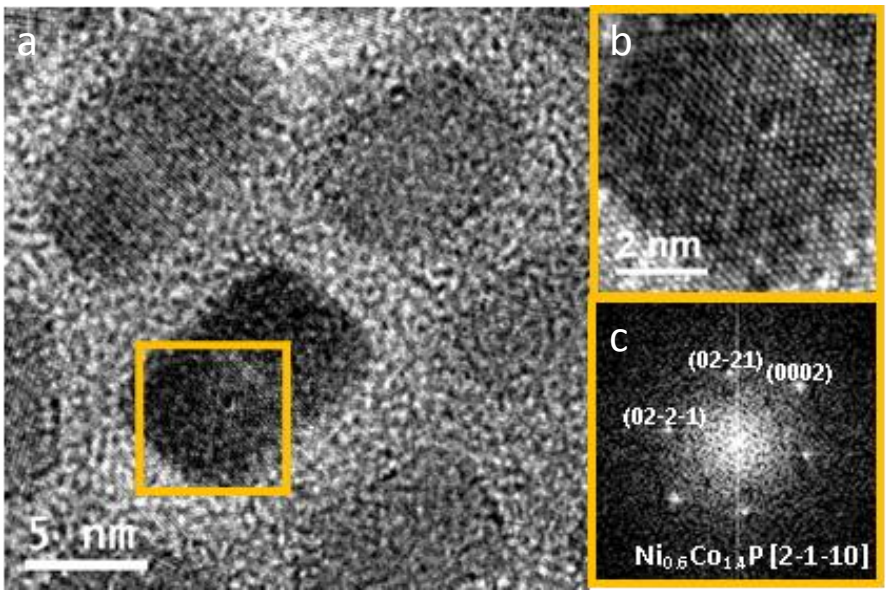

Figure S5. HRTEM micrograph of $Ni_{0.6}Co_{1.4}P$ NPs (a), detail of the NP in yellow (b) and its corresponding power spectrum (c).

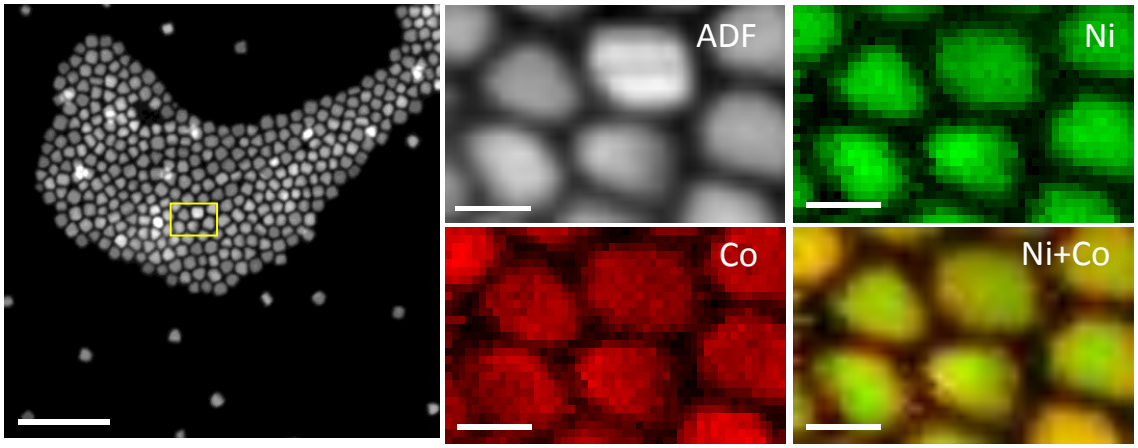

Figure S6. STEM – EELS elemental composition maps of a selected area of NiCoP nanoparticles on the left image: Ni (green), Co (red) and combination Ni+Co.

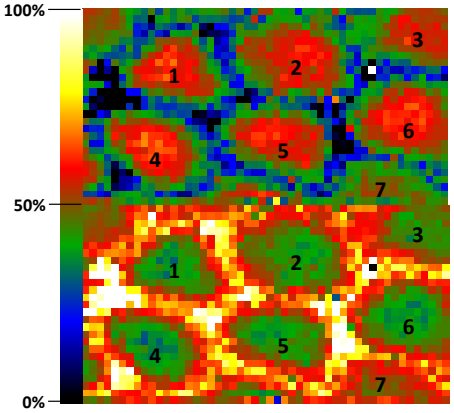

Target/Particle	Ni (%)	Co (%)	Composition
Target	*50*	*50*	*NiCo*
1	56.00	44.00	$Ni_{1.12}Co_{0.88}$
2	57.93	42.07	$Ni_{1.16}Co_{0.84}$
3	52.02	47.98	$Ni_{1.04}Co_{0.96}$
4	61.29	38.71	$Ni_{1.23}Co_{0.77}$
5	54.97	45.03	$Ni_{1.1}Co_{0.9}$
6	57.19	42.81	$Ni_{1.14}Co_{0.86}$
7	45.81	54.19	$Ni_{0.92}Co_{1.08}$

Figure S7. Ni and Co quantification maps obtained in the squared area of the STEM images in Figure S6, together with a table representing the quantification of the numbered particles.

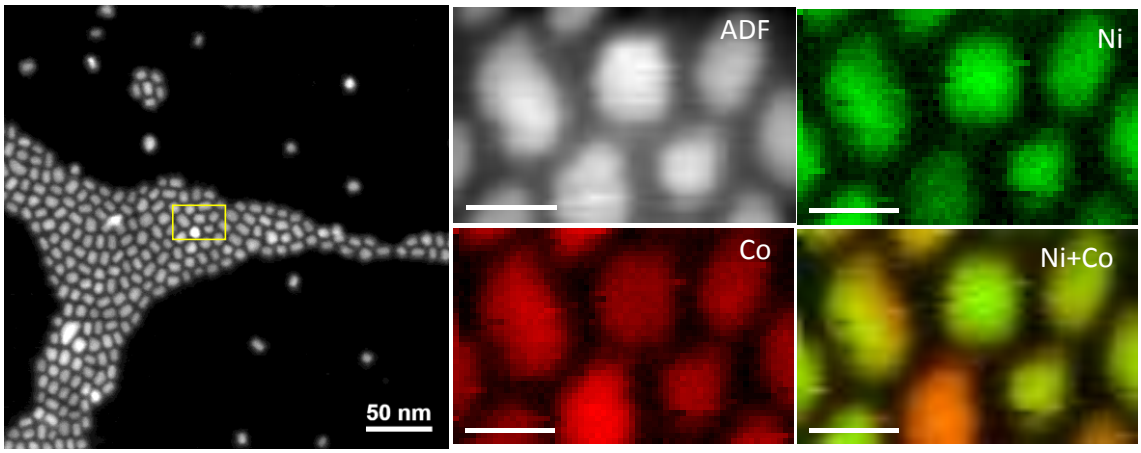

Figure S8. STEM – EELS elemental composition maps of a selected area of $Ni_{0.4}Co_{1.6}P$ nanoparticles on the left image: Ni (green), Co (red) and combination Ni+Co.

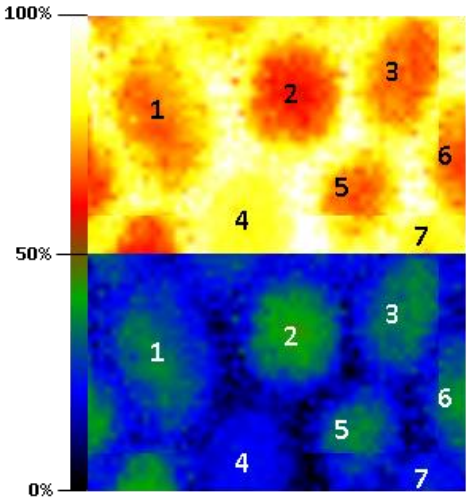

Target/Particle	Ni (%)	Co (%)	Composition
Target	*30*	*70*	$Ni_{0.6}Co_{1.4}$
1	30.02	69.98	$Ni_{0.6}Co_{1.4}$
2	37.54	62.46	$Ni_{0.75}Co_{1.25}$
3	31.54	68.46	$Ni_{0.63}Co_{1.37}$
4	17.46	82.54	$Ni_{0.35}Co_{1.65}$
5	31.58	68.42	$Ni_{0.63}Co_{1.37}$
6	32.91	67.09	$Ni_{0.66}Co_{1.33}$
7	20.67	79.33	$Ni_{0.4}Co_{1.6}$

Figure S9. Ni and Co quantification maps obtained in the squared areas of the STEM images in Figure S8, together with a table representing the quantification of the numbered particles.

4. XPS survey

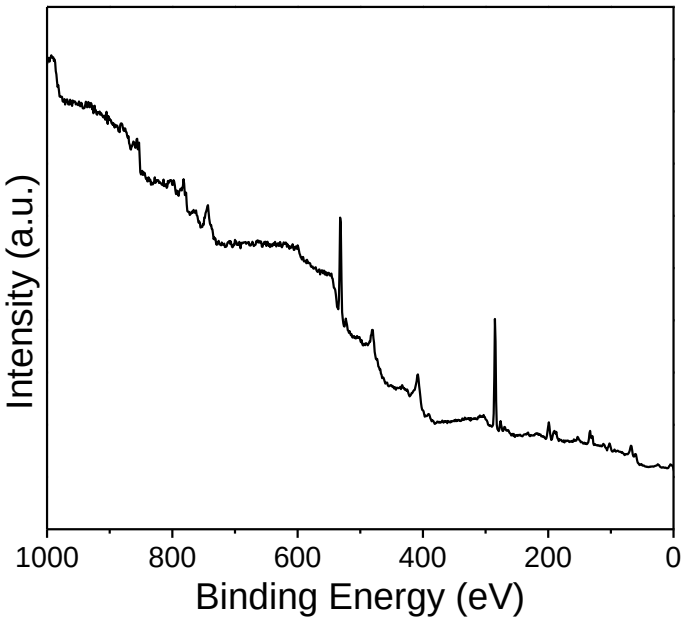

Figure S10. XPS survey of NiCoP nanoparticles.

5. Crystal structure

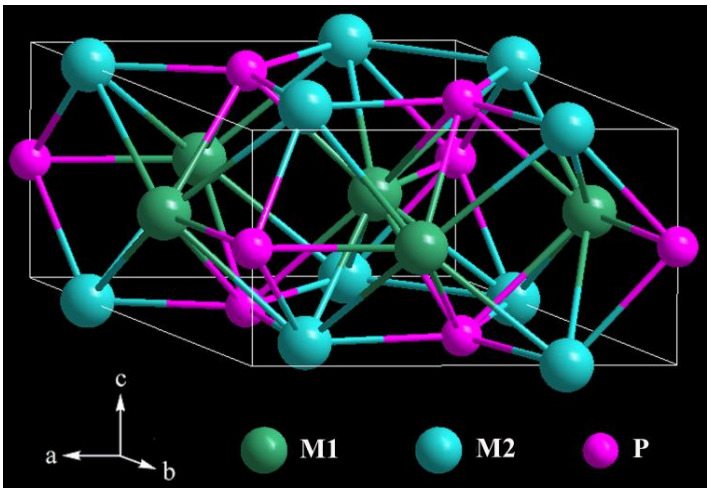

Figure S11. Hexagonal $Ni_{2-x}Co_xP$ structure type.

6. Cl-free precursor

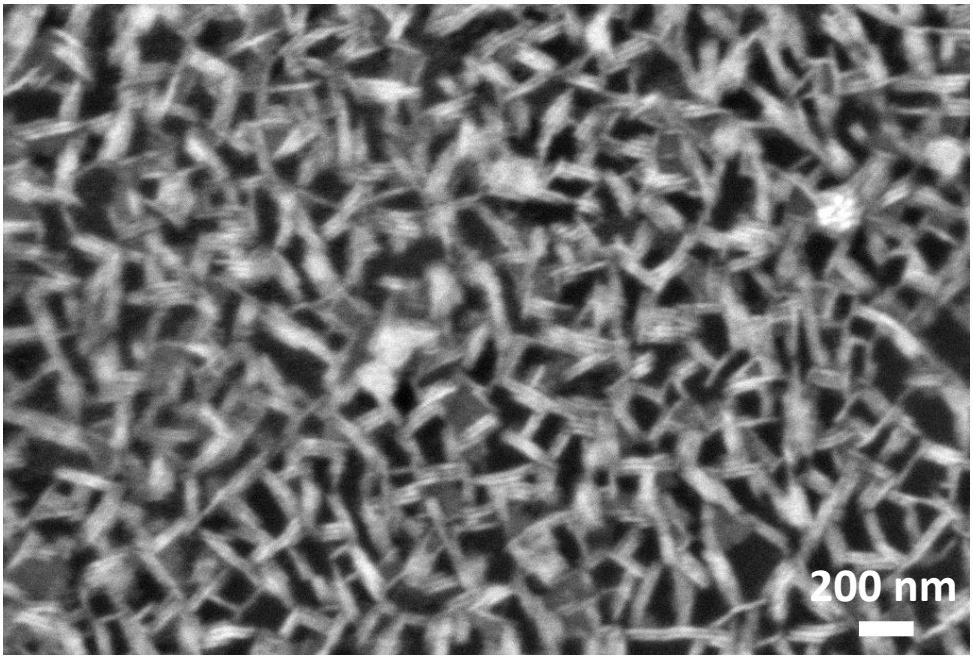

Figure S12. SEM micrograph of Co_2P nanorods obtained using $Co(NO_3)_2 \cdot 6H_2O$ instead of $CoCl_2$ as cobalt precursor ($Co(NO_3)_2 \cdot 6H_2O$: HDA : TPP = 1 : 10 : 10)

7. Stability

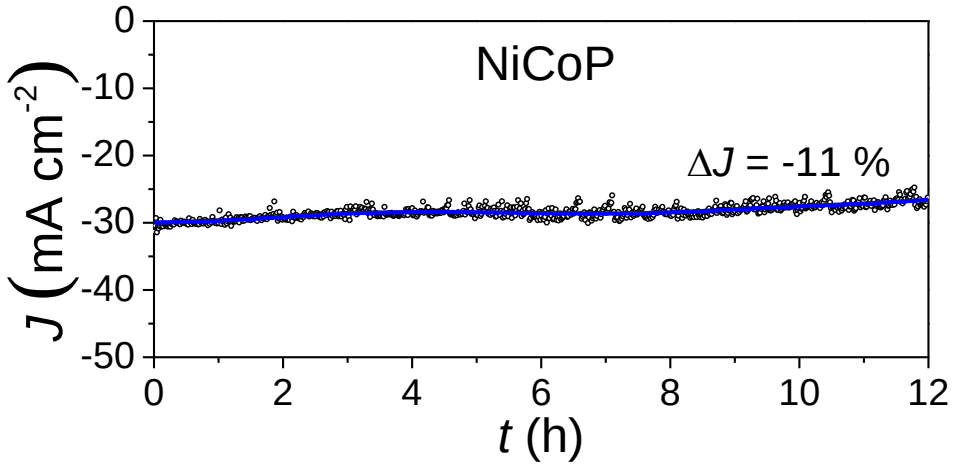

Figure S13. Time-dependent current density curve of NiCoP at an overpotential of 150 mV for 12 h.

8. Comparison of catalysts

Table S2. References of electrocatalysts for HER.

Catalyst	Substrate	Electrolyte	η at 10 mA cm^{-2}	References
MoS_2	Carbon fiber	0.5 M H_2SO_4	104	1
Mo_2C	GCE	0.5 M H_2SO_4	70	2
MoN	GCE	0.5 M H_2SO_4	125	3
MoN	GCE	1.0 M KOH	139	3
$CoSe_2$	Carbon fiber	0.5 M H_2SO_4	137	4
WS_2	GCE	0.5 M H_2SO_4	100	5
Ni_3S_2	Ni foam	1.0 M KOH	200	6
Co_2P	Ti foil	0.5 M H_2SO_4	134	7
FeP	GCE	0.5 M H_2SO_4	100	8
MoC-Mo_2C	GCE	0.5 M H_2SO_4	126	9
Fe_3C@NCNT	GCE	0.5 M H_2SO_4	154	10
Fe_3C@NCNT	GCE	1.0 M KOH	378	10
WC/graphene	Ga-W foil	0.5 M H_2SO_4	120	11
MoS_2/rGO	GCE	0.5 M H_2SO_4	120	12
$W(S_{0.48}Se_{0.52})_2$	Carbon fiber	1 M H_2SO_4	298	13
$WS_{2(1-x)}P_{2x}$	Carbon fiber	0.5 M H_2SO_4	98	14
Co_9S_8-MoS_x	Carbon fiber	0.5 M H_2SO_4	98	15
$Mn_{0.05}Co_{0.95}Se_2$	GCE	0.5 M H_2SO_4	174	16
$CoMoS_3$	GCE	0.5 M H_2SO_4	171	17
NiCoP	GCE	0.5 M H_2SO_4	97	This work

NCNT: N-doped carbon nanotubes

rGO: reduce graphene oxide

GCE: glassy carbon electrode

Table S3. References for synthesis of NiCoP.

Materials	Method	Metal precursors	P precursor	Controlled			η_{10}	Ref.
				Composition	Size	Shape		
NiCoP	Plasma-assisted	NiCo hydroxide	PH_3 gas	No	No	No	32	18
Ni-Co-P	Electro-deposition	$NiCl_2$, $Co(NO_3)_2$	NaH_2PO_2	No	No	No	30	19
NiCoP	Annealing	Ni-Co-salt	NaH_2PO_2	No	No	No	101	20
NiCoP	Annealing	Ni-Co carbonate	NaH_2PO_2	No	No	No	118	21
NiCoP	Annealing	NiCo hydroxide	NaH_2PO_2	No	No	No	124	22
NiCoP	Annealing	NiCo hydroxide	NaH_2PO_2	No	No	No	104	23
NiCoP	Annealing	$Ni_{1-0.5x}Co_{0.5x}(OH)_2$	NaH_2PO_2	Yes	No	No	59	24
NiCoP	Annealing	NiCo hydroxide	NaH_2PO_2	No	No	No	185	25
Ni-Co-P	Annealing	Ni-Co-PBA	NaH_2PO_2	No	No	No	167	26
NiCoP	Annealing	$NiCo_2O_4$	NaH2PO2	Yes	No	No	44	27
$NiCo_2P_x$	Annealing	$NiCo_2O_4$	NaH_2PO_2	No	No	No	104	28
$Ni_{0.69}Co_{0.31}P$	Annealing	$NiCoO_x$	NaH_2PO_2	Yes	No	No	100	29
NiCoP	Colloidal	$Ni(acac)_2$, $Co(acac)_2$	TOP	No	No	No	102	30
$Co_{1.6}Ni_{0.4}P$	Colloidal	$Ni(acac)_2$, $Co(acac)_2$	TOP	Yes	No	No	162	31
$Ni_{2-x}Co_xP$	Colloidal	$Ni(OAc)_2$, $Co(OAc)_2$	PPh_3	Yes	No	No	>250	32
NiCoP	Colloidal	$NiCl_2$, $CoCl_2$	TPP	Yes	Yes	Yes	97	This work

9. References

[1] J. Hu, B. Huang, C. Zhang, Z. Wang, Y. An, D. Zhou, H. Lin, M. K. H. Leung, S. Yang, *Energy Environ. Sci.* 2017, **10**, 593-603.

[2] L. Liao, S. Wang, J. Xiao, X. Bian, Y. Zhang, M. D. Scanlon, X. Hu, Y. Tang, B. Liu, H. H. Girault, *Energy Environ. Sci.* 2014, **7**, 387-392.

[3] J. Xiong, W. Cai, W. Shi, X. Zhang, J. Li, Z. Yang, L. Feng, H. Cheng, *J. Mater. Chem. A* 2017, **5**, 24193-24198.

[4] D. Kong, H. Wang, Z. Lu, Y. Cui, *J. Am. Chem. Soc.* 2014, **136**, 4897-900.

[5] L. Cheng, W. Huang, Q. Gong, C. Liu, Z. Liu, Y. Li, H. Dai, *Angew. Chem.* 2014, **53**, 7860-7863.

[6] C. Ouyang, X. Wang, C. Wang, X. Zhang, J. Wu, Z. Ma, S. Dou, S. Wang, *Electrochimi. Acta* 2015, **174**, 297-301.

[7] Z. Huang, Z. Chen, Z. Chen, C. Lv, M. G. Humphrey, C. Zhang, *Nano Energy* 2014, 9, 373-382.

[8] Y. Xu, R. Wu, J. Zhang, Y. Shi, B. Zhang, *Chem. Commun.* 2013, **49**, 6656-6658.

[9] H. Lin, Z. Shi, S. He, X. Yu, S. Wang, Q. Gao, Y. Tang, *Chem. Sci.* 2016, **7**, 3399-3405.

[10] L. Zhang, Y. Chen, P. Zhao, W. Luo, S. Chen, M. Shao, *Electrocatalysis* 2018, **9**, 264-270.

[11] M. Zeng, Y. Chen, J. Li, H. Xue, R. G. Mendes, J. Liu, T. Zhang, M. H. Rümmeli, L. Fu, *Nano Energy* 2017, **33**, 356-362.

[12] Y. Li, H. Wang, L. Xie, Y. Liang, G. Hong, H. Dai, *J. Am. Chem. Soc.* 2011, **133**, 7296-7299.

[13] K. Xu, F. Wang, Z. Wang X. Zhan, Q. Wang, Z. Chen, M. Safdar, J. He, *ACS Nano* 2014, **8**, 8468-8476.

[14] T. A. Shifa, F. Wang, K. Liu, Z. Cheng, K. Xu, Z. Wang, X. Zhan, C. Jiang, J. He, *Small* 2017, 1603706.

[15] X. Zhou, X. Yang, M. N. Hedhili, H. Li, S. Min, J. Ming, K. W. Huang, W. Zhang, L. J. Li, *Nano Energy* 2017, **32**, 470-478.

[16] Y. Liu, X. Hua, C. Xiao, T. Zhou, P. Huang, Z. Guo, B. Pan, Y. Xie, *J. Am. Chem. Soc.* 2016, **138**, 5087-5092.

[17] L. Yu, B. Y. Xia, X. Wang, X. W. Lou, *Adv. Mater.* 2016, **28**, 92-97.

[18] H. Liang, A. N. Gandi, D. H. Anjum, X. Wang, U. Schwingenschlogl, H. N. Alshareef, *Nano Lett.* 2016, **16**, 7718-7725.

[19] P. Zhang, H. Chen, M. Wang, Y. Yang, J. Jiang, B. Zhang, L. Duan, Q. Daniel, F. Li, L. Sun, *J. Mater. Chem. A* 2017, **5**, 7564-7570.

[20] X. Wang, R. Tong, Y. Wang, H. Tao, Z. Zhang, H. Wang, ACS Appl. *Mater. Inter.* 2016, **8**, 34270-34279.

[21] T. Liu, X. Yan, P. Xi, J. Chen, D. Qin, D. Shan, S. Devaramani, X. Lu, *Int. J. Hydrogen Energ.* 2017, **42**, 14124-14132.

[22] Y. Li, J. Liu, C. Chen, X. Zhang, J. Chen, *ACS Appl. Mater. Inter.* 2017, **9**, 5982-5991.

[23] J. Li, G. Wei, Y. Zhu, Y. Xi, X. Pan, Y. Ji, I. V. Zatovsky, W. Han, *J. Mater. Chem. A* 2017, **5**, 14828-14837.

[24] J. Li, M. Yan, X. Zhou, Z. Q. Huang, Z. Xia, C. R. Chang, Y. Ma, Y. Qu, *Adv. Funct. Mater.* 2016, **26**, 6785-6796.

[25] H. Zhang, X. Li, A. Hähnel, V. Naumann, C. Lin, S. Azimi, S. L. Schweizer, A. W. Maijenburg, R. B. Wehrspohn, *Adv. Funct. Mater.* 2018, 1706847.

[26] Y. Feng, X. Y. Yu, U. Paik, *Chem. Commun.* 2016, **52**, 1633-1636.

[27] C. Du, L. Yang, F. Yang, G. Cheng, W. Luo, *ACS Catal.* 2017, **7**, 4131-4137.

[28] R. Zhang, X. Wang, S. Yu, T. Wen, X. Zhu, F. Yang, X. Sun, X. Wang, W. Hu, *Adv. Mater.* 2017, 1605502.

[29] Z. Yin, C. Zhu, C. Li, S. Zhang, X. Zhang, Y. Chen, *Nanoscale* 2016, **8**, 19129-19138.

[30] C. Wang, J. Jiang, T. Ding, G. Chen, W. Xu, Q. Yang, *Adv. Mater. Inter.* 2016, **3**, 1500454.

[31] Y. Pan, Y. Chen, Y. Lin, P. Cui, K. Sun, Y. Liu, C. Liu, *J. Mater. Chem. A* 2016, **4**, 14675-14686.

[32] Q. Liang, K. Huang, X. Wu, X. Wang, W. Ma, S. Feng, *RSC Adv.* 2017, **7**, 7906-7913.